J. Fluid Mech. (2002), *vol.* 454, *pp.* 145–201.
DOI: 10.1017/S0022112001006966 Printed in the United Kingdom

Collision and rebound of small droplets in an incompressible continuum gas

By ARVIND GOPINATH AND DONALD L. KOCH

School of Chemical Engineering, Cornell University, Ithaca, NY 14853, USA

(Received 3 May 2001 and in revised form 10 August 2001)

We study the head-on collision between two weakly deformable droplets, each of radius a (in the range 10–150 μm), moving towards one another with characteristic impact speeds $\pm U_c'$. The liquid comprising the drop has density ρ_d and viscosity μ_d. The collision takes place in an incompressible continuum gas with ambient density $\rho_g \ll \rho_d$, ambient pressure p_∞' and viscosity $\mu_g \ll \mu_d$. The gas–liquid interface is surfactant free with interfacial tension σ. The Weber number based on the drop density, $We_d \equiv \rho_d U_c'^2 a/\sigma \ll 1$ and the capillary number based on the gas viscosity, $Ca_g \equiv \mu_g U_c'/\sigma \ll 1$. The Reynolds number characterizing flow inside the drops satisfies $Re_d \equiv aU_c'\rho_d/\mu_d \gg We_d^{1/2}$ and the Stokes number characterizing the drop inertia, $St \equiv 2We_d(9Ca_g)^{-1} \equiv 2(\rho_d U_c' a\mu_g^{-1})/9$ is $O(1)$ or larger.

We first analyse a simple model for the rebound process which is valid when $St \gg 1$ and viscous dissipation in both the gas and in the drop can be neglected. We assume that the film separating the drops only serves to keep the interfaces from touching by supplying a constant excess pressure $2\sigma/a$. A singular perturbation analysis reveals that when $\ln(We_d^{-1/4}) \gg 1$, rebound occurs on a time scale $t_b' = \frac{2}{3}^{1/2}\pi a We_d^{1/2} \ln^{1/2}(We_d^{-1/4}) U_c'^{-1}$. Numerical results for Weber numbers in the range $O(10^{-6}) - O(10^{-1})$ compare very well to existing experimental and simulation results, indicating that the approximate treatment of the bounce process is applicable for $We_d < 0.3$.

In the second part of the paper we formulate a general theory that not only models the flow inside the drop but also takes into account the evolution of the gap width separating the drops. The drop deformation in the near-contact inner region is determined by solving the lubrication equations and matching to an outer solution. The resulting equations are solved numerically using a direct, semi-implicit, matrix inversion technique for capillary numbers in the range 10^{-8} to 10^{-4} and Stokes numbers from 2 to 200. Trajectories are mapped out in terms of Ca_g and the parameter $\chi = (We_d/Ca_g)^{1/2}$ so that $St \equiv \frac{2}{9}\chi^2$. For small Stokes numbers, the drops behave as nearly rigid spheres and come to rest without any significant rebound. For $O(1)$ Stokes numbers, the surfaces deform noticeably and a dimple forms when the gap thickness is approximately $O(aCa_g^{1/2})$. The dimple extent increases, reaches a maximum and then decreases to zero. Meanwhile, the centroids of the two drops come to rest momentarily and then the drops rebound, executing oscillatory motions before finally coming to rest. As the Stokes number increases with Ca_g held fixed, more energy is stored as deformation energy and the maximum radial extent of the dimple increases accordingly. For $St \gg 1$, no oscillations in the centroid positions are observed, but the temporal evolution of the minimum gap thickness exhibits two minima. One minimum occurs during the dimple evolution process and corresponds to the minimum attained by the dimple rim. The second minimum occurs along the axis of symmetry when the dimple relaxes, a tail forms and then retracts. A detailed

analysis of the interface shapes, pressure profiles and the force acting on the drops allows us to obtain a complete picture of the collision and rebound process.

1. Introduction

This paper addresses binary, head-on collisions between weakly deformable liquid droplets in an incompressible gas. Our focus will be on small droplets with radii in the range $O(5) - O(100)\,\mu$m. Collisions of such small droplets are encountered in many interesting processes as diverse as rain drop formation (see for example, Fuchs 1964; Hidy & Brock 1970; Mason 1971; Brazier-Smith, Jennings & Latham 1972, and references therein), spray combustion and painting, pressurized turbines and aerosol coagulation (Friedlander 1977). For drops in this size range, the dominant factor driving collision is usually drop inertia and the impact energy involved in the collision is small compared with the surface energy associated with the gas–liquid interfaces. The velocities, shape and separation of the approaching interfaces control the hydrodynamic forces acting on the drops and determine the minimum possible distance between the drops.

When two drops collide in a gas, they may bounce apart or they may come into contact. A bounce occurs if the pressure in the gas film separating the drops deforms the drop surfaces sufficiently to transform the drops' kinetic energy into deformation energy before the gas film becomes thin enough for lubrication breakdown to occur. In this paper, we study droplet collisions that result in a bounce. The collisions are assumed to take place in an incompressible, continuum gas and so the drops undergoing collision cannot come into contact; the nature of the continuum lubrication force prevents this from occurring. We also assume that the effects of inter-particle forces such as the London–van der Waals dispersion forces are negligible. The viscosity contrast between the liquid and the gas is large enough that the gas does not slip at the interfaces. The interfaces are assumed to be tangentially immobile and this is later shown to be a good assumption.

When two rigid spheres undergo relative motion in an incompressible, continuum gas, the initial kinetic energy is dissipated by viscous forces in the gas. The force resisting relative motion scales as $O(h^{-1})$, h being the minimum gap separation. Thus, the approach is asymptotically slow. Furthermore, since there is no mechanism for energy storage, the spheres do not rebound. When two drops collide, however, the deformation of the drop surface allows for a part of the initial kinetic energy to be stored as deformation energy. This stored energy is then released when the drops slow down and transformed back into the kinetic energy of the centres of mass of the drops during the rebound process. We seek a simple theory to describe the bounce phenomenon and the dynamics in the limit of moderate to large Stokes number and small Weber number. By simultaneously including strong retarding viscous forces and also surface deformation, our work provides a rational basis to understanding and predicting collision outcomes.

The geometry of the binary encounter we study in this paper is depicted in figures 1(a) and 1(b). Both drops have the same radius a, and their centroids move with equal and opposite speeds W' (which equals U_c' when the collision begins) along the line joining their centres. The liquid comprising the drop has density ρ_d and viscosity μ_d. The collision takes place in an incompressible, continuum gas which has ambient density $\rho_g \ll \rho_d$, ambient pressure p_∞' and viscosity $\mu_g \ll \mu_d$.

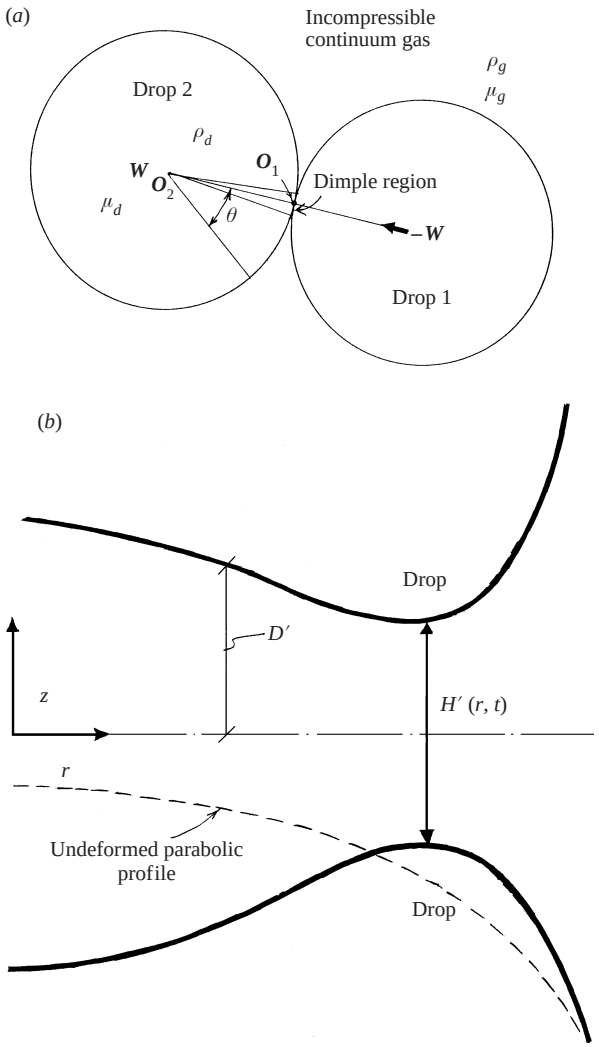

FIGURE 1. Schematic sketch showing the geometry and relative orientation for drop–drop collision. (*a*) The global geometry as viewed from a stationary reference frame whose origin, $\boldsymbol{O}_1$ is fixed on the intersection of the plane of symmetry with the line joining the drop centroids. The figure shows the origin of the accelerating reference frame, $\boldsymbol{O}_2$, fixed at the centroid of drop 2. (*b*) The local geometry of the near contact region. The solid curves represent the deformed surfaces while the dashed curve represents the interface position corresponding to a rigid drop.

The gas–liquid interface is surfactant-free and is characterized by interfacial tension σ. The parameters that we expect to influence the collision process are the Weber number based on the drop density, $We_d \equiv a\rho_d' U_c'^2/\sigma$, the Weber number based on the gas density, $We_g \equiv a\rho_g' U_c'^2/\sigma$, the capillary number based on drop viscosity, $Ca_d \equiv \mu_d U_c'/\sigma$, the capillary number based on gas viscosity, $Ca_g \equiv \mu_g U_c'/\sigma$, and the Reynolds numbers based on the drop and gas properties, $Re_d \equiv \rho_d U_c' a/\mu_d$ and $Re_g \equiv \rho_g U_c' a/\mu_g$. The collision dynamics is critically dependent on drop inertia, characterized by the Stokes number $St \equiv 2We_d(9Ca_g)^{-1}$ which is the ratio of the time over which the drops move through a distance of $O(a)$ to the viscous relaxation

Radius	a	10 μm	100 μm
Ambient pressure	p'_∞	1 atm	1 atm
Velocities	U'_c	1 cm s^{-1}	100 cm s^{-1}
Gas capillary number	Ca_g	2.5×10^{-6}	2.6×10^{-4}
Drop capillary number	Ca_d	1.2×10^{-4}	1.3×10^{-2}
Drop Weber number	We_d	1.4×10^{-5}	1.5
Gas Weber number	We_g	1.4×10^{-8}	1.5×10^{-3}
Stokes number	St	1.3	1.2×10^{3}
Drop Reynolds number	Re_d	10^{-1}	10^{2}
Gas Reynolds number	Re_g	10^{-2}	10^{1}

TABLE 1. Typical values of relevant dimensionless parameters for collisions of small water droplets in atmospheric air. The surface tension used in these estimates is 70 dyn cm^{-1}.

time based on the force exerted by the surrounding gas. Table 1 shows values of the dimensionless numbers for water droplets moving in air at velocities comparable to their terminal speeds. Note that in actual collisions, the velocity is set by external forces and so is an independent parameter. Also, typical relative velocities are less than the terminal velocities. We consider droplets of radius in the range $a = 5$–$150\,\mu$m and ranges of other parameters in typical applications are $\sigma = 20$–75 dyn cm^{-1}, $\rho_d \approx 1$ g cm^{-3} and $U'_c \approx 5$–100 cm s^{-1}. Using these values we obtain $Ca_g \sim O(10^{-6}$–$10^{-3})$, $We_d \sim O(10^{-3}$–$10^{-1})$ and $St \sim O(1$–$200)$.

Our theoretical analysis is conducted in the limits $We_d \ll 1$ and $Ca_g \ll 1$. The Stokes number characterizing the drop inertia, $St \equiv 2We_d(9Ca_g)^{-1}$ is $O(1)$ or larger. The Reynolds number based on drop properties in all cases satisfies the inequality $Re_d \gg We_d^{1/2}$. We show later that this criterion allows us to neglect viscous effects inside the drop and treat the flow as potential flow driven by the impulsive nature of the collision. The dynamics of the bounce is, to leading order, independent of the drop Reynolds number.

Experimental studies at small and $O(1)$ Weber numbers by Park (1970), Brazier-Smith (1972), Spengler & Gokhale (1973), Bradley & Stow (1978), Ochs, Czys & Beard (1980), Yao & Cai (1988), Ashgriz & Poo (1990) and Jiang, Umemura & Law (1992) indicate that the head-on collision of two small droplets at high pressures (high gas densities) result in rebound. Other experiments on off-centre binary droplet collisions by Qian & Law (1994) also show that in a highly pressurized or a high viscosity gas, collisions may result in rebound for sufficiently large impact velocities ($We_d > 1$). It is thus of interest to obtain analytical estimates of the rebound time and the associated energy loss in the complementary limit $We_d \ll 1$. Numerical investigations of drop collisions using simulation techniques have also been available for some time.

Using a marker and cell method, Foote (1975) conducted simulations of a liquid drop colliding with a wall and then rebounding. He included the effects of drop viscosity and finite surface tension. However, in his simulations, the flow and dissipation in the surrounding gas were not considered. Computations of drop collisions with a solid wall using molecular dynamics have also been reported (see, for example, Murad & Law 1999 and references therein). However, these investigations are more or less for medium to high impact energies corresponding to $We_d \geqslant 1$. More recently, Nobari, Jan & Tryggvason (1996) used simulations based on finite differences to study head-on collisions of equal sized drops moving due to a constant force. Drop

contacts were simulated artificially by removing the intervening layer at a prescribed gap width.

The extent of drop deformation is set by the imbalance between the normal stress exerted on the interface by the flow in the outside gas and the normal stress due to flow inside the drop. Typically, Re_g is $O(1)$ or only moderately small and so inertial effects in the gas are not insignificant. However, if $Ca_g \gg We_g$, or, equivalently, the Stokes number $St \ll 2\rho_d(9\rho_g)^{-1}$, viscous effects dominate in the gas. When the distance between the drop surfaces, h' is comparable to or larger than a, the drops interact very weakly and each drop experiences a force which is of the order of the Stokes drag $O(\mu_g a U_c')$. For large Stokes numbers this is insufficient to prevent the drops from approaching to distances $h' \ll a$. In fact, the energy dissipated in this outer trajectory motion is only a factor $O(St^{-1})$ of the initial kinetic energy of the drop and is negligible. Once the gap thins to very small widths, $h' \ll a$, the radial flow out of the gap leads to a viscous stress resulting in a large $O(\mu_g U_c' a/h'^2)$ lubrication force that resists drop motion and induces surface deformation. Note that the characteristic gap thickness at which drop deformation becomes important is $O(aCa_g^{1/2})$, as can be seen by balancing the viscous force exerted by the gas with the capillary pressure $O(\sigma/a)$. The criterion for the neglect of inertia of the gas when the drops are first starting to deform is $Re_g Ca_g^{1/2} \ll 1$ which is satisfied for $Ca_g \ll 1$. The small capillary number criterion implies that most of the deformation occurs only when the drops are nearly contacting. The small Weber number criterion implies that the magnitude of this deformation is small compared to the undeformed radius a, thus the drops remain spherical to leading order until the separation becomes $O(aCa_g^{1/2}) \ll a$. Therefore, detailed analysis of the relative motion at small gap separations is sufficient to determine the outcome of the collision process.

In the first part of the paper, we analyse collisions in the limits $St \gg 1$ and $Re_d \gg We_d^{1/2}$. Under these conditions, viscous dissipation in the gas and in the drop can be neglected. We assume that the film separating the drops only serves to keep the interfaces from touching by supplying a constant external pressure $2\sigma/a$. In the second part of our study, we will formulate the general theory that also includes the effects of the gas flow in the film separating the drops. The equations we obtain are then solved numerically using a matrix inversion technique and the role played by gas viscosity is investigated in detail. Wherever possible, we will compare our theoretical and numerical results to existing simulation and experimental results for droplet collisions.

2. Idealized model of the rebound process in an incompressible gas when $St \gg 1$

Collisions at Weber numbers much less than unity occur frequently and it is natural to investigate the rebound phenomena in the asymptotic limit, $We_d \ll 1$. Deformation of the interface sets in when the normal component of the stress due to flow in the drop is comparable to the rest state capillary stress due to interfacial tension. For drop separations $h' \leqslant aCa_g^{1/2}$, the lubrication pressure in the gap between the drops becomes $O(2\sigma/a)$ and the approaching surfaces deform considerably resulting in the formation of a nearly flat region. This geometry effectively traps the cushion of gas between the drops and prevents it from draining out of the gap. Clearly, the local rate at which the gas drains from this inner region depends on the local deformation. For small drop inertia, the energy stored due to deformation will be smaller or comparable

to the energy expended in forcing the gas out of the intervening gap and the drops will come to a stop and will rebound back to a very small extent. For $St \gg 1$, significant deformation will occur as the surfaces tend to deform rather than push the gas out and decrease the gap width. If the deformation is large enough, most of the initial kinetic energy is stored rather than dissipated. When the drops come to a temporary halt, the deformed surfaces will begin to relax. If this relaxation occurs on a time scale much smaller than the time it takes for the gas film to drain significantly and the viscous dissipation in the gas film is small then the drops will clearly undergo an energetic rebound. We may make the idealized assumption that the dynamics of the drop collision and rebound is independent of the rate at which the film drains and that the gas film primarily serves to prevent the drops from touching. The collision process itself, as far as the drops are concerned, is equivalent to a process where the effects of the air film are mimicked using a constant local external gas pressure that keeps the near contact region flat. In short, the gas in the gap effectively stays there, cushioning the drops from physical contact. The assumptions made in this section are all validated in the detailed calculations that include analysis of the flow in the lubricating gas film that follows in § 3.

Simulations of an idealized two-drop collision and rebound were conducted by Foote in 1975. Foote argued that the collision could be viewed as a combination of a rebound process and a film drainage process. The rebound process was studied under the assumption that the drops were prevented from touching by a constant gas pressure that constrained the two drop surfaces to meet the axis of symmetry at normal incidence (i.e. the contact angle was 180°). The area of close contact was thus nearly flat. The force acting on the drop obtained from this bounce analysis was used as an input in the film drainage problem. Based on the time for the film to drain significantly relative to the time for the drop deformation to relax, the drops could touch or bounce. Marker and cell techniques were used to solve the Navier–Stokes equations inside the drop. The flow in the surrounding gas was not considered and the simulations were conducted for Weber numbers $We_d \sim O(0.1)$–$O(10)$. Foote's results agree with previous experimental observations of drop collisions ending in rebound. The idealized model of the rebound process we consider is the same as that simulated by Foote. Our analytical results for $We_d \ll 1$ complement Foote's simulations for $We_d \sim O(1)$ and provide us with quantitative details of the flow and rebound dynamics. Comparison to Foote's results indicates that the analytical theory is valid for Weber numbers of up to 0.3. We will also compare our predictions with experimental results by Park (1970) on water droplets colliding in humidified nitrogen at atmospheric pressure and observations of drops colliding with an air–water planar interface by Jayaratne & Mason (1964).

The scalings for the bounce time derived in this section can also be used to predict the collision and bounce of small liquid droplets with hot rigid walls well above the Leidenfrost temperature. The Leidenfrost temperature is the wall temperature at which the total evaporation time of a droplet is the longest. The Leidenfrost temperature has long been taken as the criterion to identify characteristic regimes for hydrodynamic impact patterns for droplets impinging on a heated wall and is also sometimes considered as the lowest boundary of the non-wetting impact. Experimental observations by Karl & Frohn (2000) and Yao & Cai (1988) using high-speed video photography show that collisions of small droplets of radii $O(10$–$100)\,\mu$m with rigid walls at $We_d \sim O(1)$ are almost elastic, with the drop undergoing very small deformations. Since the collision occurs above the Leidenfrost temperature, the liquid does not wet the wall at small enough velocities and the vaporization of some of the liquid comprising the drop may be neglected.

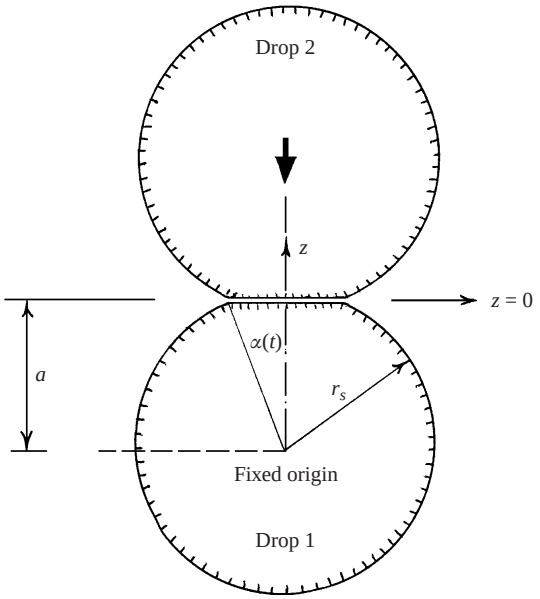

FIGURE 2. Schematic sketch showing the geometry and relative orientation for the idealized drop–drop collision. The area of near-contact is approximated by a flat region whose radial extent varies with time. The drop separation in this dimple region is assumed to be constant and very small compared with the characteristic magnitude of the drop interface deformation.

2.1. *Governing equations and scaling results*

Owing to the cylindrical geometry and symmetry inherent in the collision orientation, we choose to study the effects of the collision on drop 1. We consider a spherical coordinate system that is fixed in space and time in the interior of drop 1, such that the origin lies at a distance a from the plane of symmetry along the line of centres, as illustrated in figure 2. Thus, as the drop collision proceeds, the centres of mass of each drop move relative to this fixed origin. We neglect flow in the gas completely, so neither the density nor the viscosity of the gas play any role. The only dimensionless parameters that affect the dynamics are the Weber and Reynolds numbers based on drop properties, namely, We_d and Re_d. The main quantities of interest are the time scale over which the drops bounce and the extent of the flat radial dimple region as a function of time.

For gap separations of $O(a)$ and $St \gg 1$, the force exerted by the gas is small and causes negligible deformation. The deformation only becomes significant when the separation becomes $O(a\kappa)$ (we show later in this paper that $\kappa \sim O(Ca_g^{1/2})$). For drop separations much greater than $O(a\kappa)$, the drops may thus be considered spherical. As the surfaces approach, the fluid in the film drains owing to the radial flow induced in the gap thus exerting a normal force resisting drop motion. When the separation becomes $O(a\kappa)$, the confined air film leads to a strong localized pressure that flattens the approaching surfaces. Let the centre of mass speed of each drop at a separation of $O(a\kappa)$ be U_c'. The kinetic energy is thus $O(\rho_d a^3 U_c'^2) = O(We_d \sigma a^2)$. Since viscous dissipation in the gas is negligible, most of this initial kinetic energy of the drops is stored as surface deformation energy during the course of collision. At some point in the collision process, the centres of mass of the drops reverse their direction of motion and the drops begin to rebound. The deformation energy is transformed back

into kinetic energy and the rebound process is complete when the drops are again separated by a distance large compared to $O(a\kappa)$.

For the deformation energy to balance the $O(\frac{4}{3}\pi\rho_d a^3 U_c'^2)$ initial kinetic energy, the characteristic magnitude of the interface deformation should scale as $O(aWe_d^{1/2})$. The pressure exerted in the dimple region is $2\sigma/a$. The time scale for the drops to translate through a distance of $O(a)$ is $O(a/U_c')$ whereas the time for the deformation to relax is much smaller being $O(aWe_d^{1/2}U_c'^{-1})$. This is also the time over which the centre of mass velocity changes sign and the rebound occurs. Balancing the overall force with the rate at which the centre of mass velocity changes indicates that the radial extent of the dimple scales as $O(aWe_d^{1/4})$. This scaling is thus consistent with the $O(aWe_d^{1/2})$ deformation and the $O(aWe_d^{1/2})$ distance the centroid of the drops translate through during the bounce.

The flow field inside the drop may be described by the Navier–Stokes equation supplemented with the criterion that the velocity field is divergence free. We scale all lengths with the undeformed drop radius a, drop velocity with the characteristic velocity of approach when collision begins, U_c' and time with $aWe_d^{1/2}U_c'^{-1}$. For collisions of interest, drop Reynolds numbers are usually greater than one and the Weber number is very small, so viscous effects are negligible. Furthermore, since $St \gg 1$, we anticipate that the dynamic pressure in the drop will scale as $O(\rho_d U_c'^2 We_d^{-1/2})$ and use this as the characteristic deformation-induced dynamic pressure. The Navier–Stokes equation for the fluid velocity $\boldsymbol{u}$ and pressure p_d in the drops reads:

$$\frac{\partial \boldsymbol{u}_d}{\partial t} + We_d^{1/2}\boldsymbol{u}_d \cdot \nabla \boldsymbol{u}_d = -\nabla p_d + \frac{We_d^{1/2}}{Re_d}\nabla^2 \boldsymbol{u}_d + \frac{We_d^{1/2}}{Fr}\boldsymbol{g} \tag{2.1}$$

where in equation (2.1), $Fr \equiv U_c'^2/ag$ is the Froude number and $\boldsymbol{g}$ is the unit vector along which gravity (of magnitude g) acts. In most collisions of interest, $We_d^{1/2}/Re_d \ll 1$, i.e. the $O(a^2\rho_d/\mu_d)$ time scale for viscous diffusion of momentum in the drop is much larger than the $O(aWe_d^{1/2}/U_c')$ bounce time. The Froude number is typically large for these collisions because the fluid acceleration is greater than g during most of the collision. Taking the terminal velocity as a typical relative velocity indicates that the Froude number is large whenever the Stokes number is large. Thus, we will neglect gravity in our analysis, i.e. we set the Froude number to infinity. Since the gravity term is absent and the viscous term is typically negligible compared to the inertia terms, the equation of motion reduces to the unsteady, linear form:

$$\frac{\partial \boldsymbol{u}_d}{\partial t} = -\nabla p_d. \tag{2.2}$$

The pressure gradient generated in the drop due to the impulsive nature of the collision is balanced by drop inertia. Note that all velocities, forces and position vectors are measured in the stationary inertial reference frame.

The fluid in the drop undergoes inviscid impulsive motion owing to the deformation of the bounding surface. This deformation produces instantaneous pressure gradients which cause instantaneous changes in the fluid velocity. The initial state is assumed to be an undeformed drop so that the initial vorticity is everywhere zero. The traction generated by the ambient gas on the drop surface is a source of vorticity. When $Re_d \gg 1$, the effect of these tangential stresses is confined to a very small boundary layer of $O(aRe_d^{-1/2}We_d^{1/4})$ close to the surface during the $O(aWe_d^{1/2}U_c'^{-1})$ time it takes for the bounce to occur. Thus, we may assume that the flow in the interior of the drop

is irrotational. Furthermore, the pressure drop across this boundary layer generated due to viscous effects is small compared to that generated by the impulsive motion of the drop. Equation (2.1) also indicates that the viscous terms are in fact less important than the nonlinear inertial terms when $Re_d \gg We_d^{1/2}$. Consequently, we expect drop viscosity to have negligible effects on the rebound process.

In the analysis that follows, we will assume that there is a localized pressure of $O(2\sigma/a)$ acting over a flat region of angular extent α. Thus, the gas pressure can be written as

$$p'_g = p'_\infty + 2\frac{\sigma}{a}H(\alpha - \theta),$$

$H(z)$ being the Heaviside step function. Equation (2.2) allows us to write the pressure inside the drop in the form:

$$p'_d = p'_\infty + 2\frac{\sigma}{a} + A'(t) - \rho_d\left(\frac{\partial\phi'}{\partial t'}\right)_s,$$

where $A'(t)$ is a function of time. The $O(aWe_d^{1/2})$ surface deformation is caused by the localized pressure $2\sigma/a$ acting in the region around the centreline. Initially, when the undeformed drops begin their approach, the angular extent of the dimple region, α, is zero. As the drops come closer, the pressure flattens an increasing portion of the surface and hence the radial extent will evolve with time.

We now write the velocity field as the gradient of a potential function, ϕ which satisfies Laplace's equation,

$$\boldsymbol{u}_d = \nabla\phi.$$

Thus,

$$\nabla^2\phi = 0, \tag{2.3}$$

owing to the incompressibility of the fluid in the drop. To see this, we note that there are no sources of mass or momentum inside the drop. Equation (2.3) also implies that

$$\int_{V_d} \nabla^2\phi \,\mathrm{d}V_d = 0 = \int_{\mathscr{A}_d} ((\nabla\phi)_s \cdot \boldsymbol{n}_s)\,\mathrm{d}\mathscr{A}_d$$

where V_d and $\mathscr{A}_d$ stand for the volume and surface of the drop, respectively. As far as the fluid inside the drop is concerned, the flat dimple region looks like a point since its radial extent is only $O(aWe_d^{1/4})$ compared to the $O(a)$ extent of the drop. The development of the flat region displaces a mass of fluid that is $O(\rho_d a^3 We_d)$. This is an $O(We_d)$ fraction of the total mass of the drop. In the analysis that follows, we will enforce the volume constraint in the drop to $O(We_d^{1/2})$ with errors of $O(We_d)$ and so the effects of this flat region can be neglected in formulating the equation for the velocity potential in the drop. We also note that the near-contact region is assumed to remain flat. Hence, as the centroids of the drops become closer to each other, in order to keep the volume constant, the drops bulge at their equators.

Without loss of generality, we may set the constant $A'(t)$ to zero for all time. This is permitted since ϕ and $\mathrm{d}\phi/\mathrm{d}t$ are defined to arbitrary constants which may be chosen to make $A'(t)$ zero. This result is also obtained by matching ϕ in the outer and inner regions. The most general solution for the velocity potential is thus a linear superposition of growing spherical harmonics. Note that ϕ and its derivatives have to be finite at the origin of the spherical coordinate system. The boundary conditions that must be imposed are the kinematic condition at the drop interface,

$$(\nabla\phi)_s \cdot \boldsymbol{n}_s = \boldsymbol{U}_s \cdot \boldsymbol{n}_s, \tag{2.4}$$

where $\boldsymbol{n}_s$ is the outward unit normal at the drop surface (represented by s). This imposes the constraint that the interface is a material surface and fluid elements on the interface remain on it at all times. Since the only normal stresses are due to the liquid and gas pressures, the normal stress balance reduces to the Young–Laplace equation,

$$(p'_d - p'_g)_s = \sigma(\nabla' \cdot \boldsymbol{n}')_s. \tag{2.5}$$

Let $\boldsymbol{r}^*$ be the position vector of a point as measured from the fixed origin (in the interior of drop 1) and $\eta = \cos\theta$. Then we have,

$$r^*_s(\eta, t) = aR(\eta, t) = a[1 + We_d^{1/2}\mathscr{H}(\eta, t)].$$

The expression on the right-hand side of equation (2.5), i.e. the curvature term representing the pressure drop across the interface due to surface tension, may then be written in dimensionless form as:

$$\Upsilon R = \frac{-([(1-\eta^2)R_\eta]_\eta - 2R)R + \eta(1-\eta^2)[R_\eta^3 R^{-1}] + 3(1-\eta^2)(R_\eta)^2}{[R^2 + (1-\eta^2)(R_\eta)^2]^{3/2}},$$

the subscripts η denoting differentiation with respect to η. Substituting the expression for R we obtain the much simplified linearized form for the curvature term valid for small deformations:

$$\Upsilon_o\mathscr{H} = -2\mathscr{H} - \frac{\mathrm{d}}{\mathrm{d}\eta}\left[(1-\eta^2)\frac{\mathrm{d}\mathscr{H}}{\mathrm{d}\eta}\right].$$

The axisymmetric collision geometry and the structure of the operator Υ_o indicate that we can write $\mathscr{H}$ as (see Appendix A):

$$\mathscr{H}(\eta, t) = \sum_{k=0}^{\infty} D_k(t)\mathscr{P}_k(\eta), \tag{2.6}$$

where $\eta = \cos\theta$ and $\mathscr{P}_k(\eta)$ is the Legendre function of order k. Imposition of the constraint that the drop volume is constant at all times, shows that the mode corresponding to a uniform volumetric change, $D_o(t) = 0$. Also, the velocity of the centre of mass of the drop is given by $\mathrm{d}D_1/\mathrm{d}t$ and the rate at which this changes is related to the overall force acting on the drop.

The size of the transition region intermediate between the dimple and outer regions may be estimated easily as $O(aCa_g^{1/4})$. For the inner region to be approximately flat, we require that the $O(a^2\sin^2\alpha/\kappa)$ radius of curvature of the dimple be much larger than a. Finally, we note that the area of the transition region over which the curvature changes from infinity to a value of $O(a^{-1})$ is given by $O(aCa_g^{1/4})$ and is much less than the $O(aWe_d^{1/4})$ size of the flat region.

Geometric considerations indicate that the area of closest approach may be approximated as a circle and so α, the half-angle subtended by the flat region at the drop centre, is given by:

$$1 + We_d^{1/2}\sum_{k=1}^{\infty} D_k(t)\mathscr{P}_k(\cos\alpha) = (\cos\alpha)^{-1}. \tag{2.7}$$

Let $\boldsymbol{e}_r$ and $\boldsymbol{e}_\theta$ be the unit surface vectors along the radial and tangential directions, respectively. Using, $\boldsymbol{n}_s \approx \boldsymbol{e}_r + O(We_d^{1/2})\boldsymbol{e}_\theta$, we can write the radius of curvature as:

$$(\nabla' \cdot \boldsymbol{n}')_s = \frac{2}{a} + \frac{1}{a}We_d^{1/2}\sum_{k=1}^{\infty}(k^2 + k - 2)D_k(t)\mathscr{P}_k(\eta).$$

The solution for ϕ valid away from the inner flat region which satisfies the symmetry conditions and is bounded for all points within the drop is given by

$$\phi = \sum_{k=0}^{\infty} B_k (r^*)^k \mathscr{P}_k(\eta). \tag{2.8}$$

Substituting (2.6) and (2.8) in the kinematic condition (2.4), and using the orthogonality properties of Legendre polynomials gives us one relationship between $B_k(t)$ and $D_k(t)$ valid for $k \geqslant 1$:

$$\frac{\mathrm{d}D_k}{\mathrm{d}t} = kB_k. \tag{2.9}$$

The second equation relating the two sets of unknown coefficients can be obtained by substituting the expansions for the deformation and velocity potential in the normal stress boundary condition. This gives us the Young–Laplace equation of the form ($k \geqslant 1$):

$$\frac{\mathrm{d}B_k}{\mathrm{d}t} = -We_d^{-1/2}[\mathscr{P}_{k-1}(\cos\alpha) - \mathscr{P}_{k+1}(\cos\alpha)] - [k(k+1) - 2]D_k. \tag{2.10}$$

Equations (2.9) and (2.10) along with equation (2.7) for the extent of the inner region serve to define the problem fully. Thus, the force in the inner region drives a potential flow inside the drop which then controls surface deformation and the extent of the flat region.

Tsao & Koch (1994) studied the rebound process for low-Weber-number, high-Reynolds-number bubbles colliding in a liquid to which ionic salts have been added. The addition of dissociating salts creates a strong hydration repulsive force that acts when the bubbles are nearly touching and keeps the near-contact interfaces separated (thus this repulsive force is analogous to the force exerted by the pressure in the gas film). The inertia of the liquid outside the bubbles was taken into consideration and the flow outside the bubbles was modelled using potential flow theory. The qualitative behaviour of the drop bounce is similar to that of the bubble bounce, in fact, when $\ln(We_d^{1/4}) \gg 1$, the analytical expressions for the bouncing times and the radial extent of the dimple region are the same. This is essentially due to the potential flow formulation.

As $We_d \to 0$, we anticipate that more modes must be included for accurate numerical resolution of the deformation. Combining equations (2.9) and (2.10) gives us the following second-order differential equation for $D_k(t)$:

$$\frac{\mathrm{d}^2 D_k}{\mathrm{d}t^2} = -k[k(k+1) - 2]D_k - kWe_d^{-1/2}[\mathscr{P}_{k-1}(\cos\alpha) - \mathscr{P}_{k+1}(\cos\alpha)], \tag{2.11}$$

for $k \geqslant 1$. Analysis of the $k \gg 1$ modes shows that for $1 \ll k \ll \alpha^{-1}$,

$$D_k \approx -We_d^{-1/2}\left[\frac{2k+1}{2k^2}\left(\alpha^2 - \frac{\alpha^4}{12}\right) - \frac{k(k+1)(2k+1)}{16k^2}\alpha^4\right], \tag{2.12}$$

and for $k \gg \alpha^{-1}$

$$D_k \approx -\frac{We_d^{-1/2}}{k^{5/2}}\left(\frac{8\sin\alpha}{\pi}\right)^{1/2}\sin[(k+\tfrac{1}{2})\alpha - \tfrac{1}{4}\pi]. \tag{2.13}$$

Thus, for a fixed value of the Weber number, $k\alpha \ll 1$, $D_k \sim k^{-1}$ and for $k\alpha \gg 1$, D_k decays faster than $O(We_d^{-1/2}\sin\alpha^{1/2}k^{-5/2})$. Note that when $k \sim O(\alpha^{-1})$, the deformation

D_k is $O(\alpha)$. We would need to keep terms $k \sim O(We_d^{-1/4})$ to describe the deformation close to the inner region. Equation (2.11) indicates that higher-order deformation modes have a leading $O(k^{-2})$ component that is in quasi-equilibrium with the forcing pressure, namely, the $[\mathscr{P}_{k-1}(\cos\alpha) - \mathscr{P}_{k+1}(\cos\alpha)]$ term. These modes also have a small $O(k^{-3})$ component that oscillates with a large $O(k^{3/2}/2\pi)$ frequency. For very small Weber numbers, the time scale of the bounce is much larger than the period of oscillation of these high-frequency components and hence the large modes of surface deformation are essentially in equilibrium with the driving force.

We note that the initial-value problem of determining the droplet deformation and the evolution of the interface shape with time is, in principle, solvable using a known set of eigenvalues and the associated normal modes for each value of the Weber number. The deformation can be written as a linear superposition of the corresponding non-degenerate eigenvalues. Clearly, in the case of zero net force (i.e. the dimple extent is always zero), the free-surface oscillations are solely due to capillary effects with the net surface energy being conserved.

2.2. *Analytical solutions when* $\ln(We_d^{-1/4}) \gg 1$

The equations described in the previous section are obtained by neglecting higher-order terms thus leading to algebraic errors of $O(We_d^{1/4})$. A completely analytical approach, albeit with larger logarithmic errors is possible when $\ln(We_d^{-1/4}) \gg 1$. However, comparison of results obtained by this asymptotic analysis to the exact numerical and simulation results shows the approximate theory to be valid over a surprisingly large range of Weber numbers.

Expressions (2.6) and (2.12) indicate that the sum of the deformation modes $1 \ll k \ll We_d^{-1/4}$ gives a logarithmic term of $O(\ln(We_d^{-1/4}))$ for the scaled deformation. In other words, as the Weber number becomes asymptotically small, the length scale of the translational mode is different from that of the other surface deformation modes by a logarithmic factor. Thus, the flow driven by deformation modes can be neglected when compared to that driven by the primary translational mode. The main variable controlling the dynamics is the instantaneous force acting on the drop that tends to change its centre of mass velocity. In view of these observations, we now rewrite the equation for the position vector on the drop surface as follows:

$$r_s(\eta, t) = 1 + \delta_1 D_1^*(t)\mathscr{P}_1(\eta) + \delta_2 \sum_{k=2}^{\infty} D_k^*(t)\mathscr{P}_k(\eta). \tag{2.14}$$

Here, δ_1 and δ_2 are small parameters which were assumed to be equal to $We_d^{1/2}$ in our previous analysis. Consider the energy balance that describes the conversion of initial kinetic energy of the drop into deformation energy. The total energy stored as surface deformation energy is the area integral of the sum of the deformation modes. For all the initial kinetic energy to be stored as deformation energy, this area integral should be $O(We_d)$. A rough argument assuming that all modes scale similarly would indicate that deformation modes are $O(We_d^{1/2})$, thus giving the $O(We_d)$ estimate for the energy stored as deformation energy. For asymptotically small Weber numbers, the equations obtained previously indicate that the sum of modes $k \gg 1$ gives a term that is $O(\ln(We_d^{-1/4}))$ larger than expected. This means the magnitude of these higher modes should be $O([We_d/\ln(We_d^{-1/4})]^{1/2})$ instead of $We_d^{1/2}$ to obtain the correct global energy scaling. We thus see that to leading order, $\delta_1/\delta_2 \sim \ln(We_d^{-1/4}) \gg 1$. Equating the inertia of the drop to the net force exerted by the localized pressure

gives $\delta_1\delta_2 = We_d$. Analytical expressions for δ_1 and δ_2 can be obtained by combining the scaling from the force balance with the scaling from the surface energy balance. This yields

$$\delta_1 = We_d^{1/2} \ln^{1/2} We_d^{-1/4} \left[1 + O\left(\frac{\ln^{1/2}\ln^{1/4} We_d^{-1/4}}{\ln^{1/2} We_d^{-1/4}}\right)\right].$$

and

$$\delta_2 = \frac{We_d^{1/2}}{\ln^{1/2} We_d^{-1/4}} \left[1 + O\left(\frac{\ln^{1/2}\ln^{1/4} We_d^{-1/4}}{\ln^{1/2} We_d^{-1/4}}\right)\right].$$

The extent of the inner flat region is obtained from force balance arguments and is $O(\delta_2^{1/2})$. Re-scaling the time for the bounce by $aU_c'^{-1}\delta_1$ and using (2.8) and (2.14) in (2.4) we obtain:

$$\frac{\mathrm{d}D_1^*}{\mathrm{d}t_*} = B_1, \quad \frac{\delta_2}{\delta_1}\frac{\mathrm{d}D_k^*}{\mathrm{d}t_*} = kB_k \quad (\forall\ k \geqslant 2). \tag{2.15}$$

The deformation modes $1 \ll k \ll \alpha^{-1}(t_*)$ are in quasi-steady equilibrium with the forcing in the inner region and are given by:

$$D_k^*(t_*) \approx -\frac{\alpha_*^2(t_*)}{k} + O\left(\frac{1}{k^2}\right), \tag{2.16}$$

where, α_* is the scaled radial extent of the inner region written thus:

$$\alpha_*(t_*) = \alpha(t_*)\left[\frac{We}{\delta_1}\right]^{-1/2} = \alpha(t_*)\delta_2^{-1/2}$$

An overall force balance on the drop gives

$$\frac{\mathrm{d}^2 D_1^*}{\mathrm{d}t_*^2} = \frac{\mathrm{d}B_1}{\mathrm{d}t_*} = -\tfrac{3}{2}\alpha_*^2(t_*). \tag{2.17}$$

The same result can be obtained by simplifying the normal stress balance, namely, the Young–Laplace equation. The radial extent of the inner region is coupled directly to the translational mode since the other modes of fluid motion driven by the deformation are small in the limit $We_d \to 0$. The fluid motion inside is primarily controlled by the local applied pressure (forcing). In the limit of small α, the radial extent is determined to leading order by the translation mode and also the sum of higher-order modes. Indeed, a Taylor series expansion of (2.7) for small α indicates that:

$$\alpha_*^2(t_*) = D_1^*(t_*). \tag{2.18}$$

The contribution from modes $k \gg 1$ is as important as that from the $k = 1$ mode, but much larger than that from other $k \sim O(1)$ modes. The bounce time defined as the time it takes for the drops to rebound back to their initial separation is given by

$$t_b' = \pi\sqrt{\tfrac{2}{3}}aU_c'^{-1}\delta_1. \tag{2.19}$$

Using the initial conditions for the deformation and flow modes, we obtain the functional forms for B_1 and D_1^*:

$$B_1(t_*) = \cos\left(\sqrt{\tfrac{3}{2}}t_*\right), \quad D_1^*(t_*) = \sqrt{\tfrac{2}{3}}\sin\left(\sqrt{\tfrac{3}{2}}t_*\right) \tag{2.20}$$

Thus,

$$D'_{1,max} \approx \sqrt{\tfrac{2}{3}} a We_d^{1/2} \ln^{1/2}(We_d^{-1/4}). \tag{2.21}$$

The total dimensional force, $F'(t')$, acting on the drop from the $2\sigma/a$ pressure acting over the flat region of radial extent $\alpha(t_*)$ is:

$$F'(t') = 2\pi\rho_d U'_c 2a^2\delta_1^{-1}\alpha_*^2(t') \sim O\left(2\frac{\sigma}{a}a^2\delta_1\right). \tag{2.22}$$

Clearly, in this asymptotic limit, the maximum force occurs when the flat region has the maximum radial extent. We also note that the localized force is assumed to be independent of the drop velocity. As the collision proceeds, the initial kinetic energy of the drop is converted to the surface deformation energy, kinetic energy of the fluid and work done against the force. However, in the limit $\ln(We_d^{-1/4}) \gg 1$, the force is approximately simple harmonic in nature and is hence conservative. This leading-order approximation indicates that all the energy expended in deforming the surface is converted back to the kinetic energy of the drop when the collision is complete. This, however, is only an approximation as the rebound process and approach are not symmetric when $k \sim O(1)$ modes are considered and this asymmetry becomes more pronounced as the Weber number increases. The kinetic energy at time $t = 0$ is $\frac{2}{3}\pi\rho_d a^3 U'^2_c$. At any arbitrary time during the approach or rebound, the kinetic energy in the fluid is given by:

$$E'_{KE} = \tfrac{1}{2}\rho_d \int_{V'_d} (\nabla'\phi')^2 \, \mathrm{d}V'. \tag{2.23}$$

Using the analytical expressions obtained in this section, we can write

$$\frac{E'_{KE}(t_*)}{E'_{KE}(0)} = \cos^2\left(\sqrt{\tfrac{3}{2}}t_*\right). \tag{2.24}$$

2.3. *Numerical results and comparison with existing simulations and experiments*

The first-order differential equations (2.9) and (2.10) in conjunction with the algebraic equation (2.7) can be solved simultaneously to obtain the deformation and fluid modes. We start the collision when the drops are separated by a distance equal to $2a$. The initial conditions are taken to be:

$$D_{k\geqslant 1}(t=0) = 0, \quad B_{k\geqslant 2}(t=0) = 0, \quad B_1(t=0) = 1.$$

The dimensionless centre-to-centre distance between the drops at any instant in time is given by $2(1 - We_d^{1/2} D_1(t))$.

Numerical solutions were obtained as follows. We chose a value of N^* and retained terms $1 \leqslant k \leqslant N^*$ in the expansions to obtain a finite system of equations for the unknown coefficients. The resulting equations were solved by a second-order predictor–corrector method. The value of N^* was varied until convergent results (within variations of 1%) were obtained for the variables of interest. The temporal evolution of the drop deformation, fluid motion and dimple extent was followed. Finally, the calculations were terminated when the drop reached its initial position, i.e. the drops were separated by a distance equal to $2a$. This procedure was repeated for various values of the Weber number.

The equations for D_k indicate that a very large number of nodes $k \sim O(We_d^{-1/4})$ are required to resolve accurately the deformation and fluid flow inside the drop. As $We_d \to 0$, we would need to solve a very large and stiff set of nonlinear equations. In order to avoid this, we use expressions (2.12) and (2.13) to simplify the numerical solution. We split the set of equations into two sets: the first for

$1 \leqslant k \leqslant N = \sim O(We_d^{-1/4})$ and the other for $k \geqslant N$. For the latter equations, we use the asymptotic expressions for D_k presented earlier while explicitly solving for the deformation modes for $1 \leqslant k \leqslant N$. This procedure was used to obtain results for Weber numbers less than 10^{-4}. For Weber numbers $O(10^{-4})$–$O(10^{-3})$, we used the asymptotic expressions and also solved the system using a large number of modes. Both methods yield identical results.

The radial flow in the drop induced by the flattening of the near-contact surfaces causes the surface to oscillate. This leads to disturbances that propagate to the top of the drop. The whole drop deforms to an $O(aWe_d^{1/2})$ extent and the surface oscillates as the collision proceeds. The top of the drop also undergoes flattening and attains a large curvature. This may be seen from figure 3(*a*) which shows the shape of drop 1 when the dimple is at its maximum extent for a Weber number of 10^{-3}. The drop is seen to be spheroidal with a bulging centre. Small Weber number drops undergo nearly elastic collisions. Thus, at lower Weber numbers, we would expect that the surface deformation resulting from the radial flow occurring owing to the collision has time to propagate along the surface as a capillary wave and thus result in long wavelength surface disturbances. The rebound occurs owing to the relaxation of the drop deformation and owing to the large pressure gradient that develops across the interior of the drop. Our results indicate that at larger impact speeds, drops of the same radii undergo a larger deformation. They reach their maximum deformation sooner and also the time for bounce decreases. We observe that the time scale of the bounce is very close to twice the time needed for the drop to attain its state of minimum kinetic energy. For collisions characterized by $O(1)$ We_d, Wachters & Westerling (1966) find that rebound can take significantly longer owing to the long time necessary for the deformed shape the drop attains to relax, relative to the time for the deformation from an initial spherical shape. This tendency persists for the case of small Weber number. As the surface deformation leads to surface oscillations, the period of the lowest mode of oscillation is the Rayleigh mode characterized by the Rayleigh time scale, $\tau_R \sim O(aU_c'^{-1}We_d^{1/2})$. Foote's numerical results showed that this was indeed the case but his calculations also indicated that the time scale of the bounce divided by the Rayleigh time scale seemed to diverge as $We_d \to 0$; our analysis in § 2.2 predicts that the sum of the deformation modes leads to a logarithmic factor that accounts for the divergence.

Consider the temporal behaviour of the centre of mass velocity. The drops initially have velocities ± 1. As the drops move towards each other owing to inertia, they also decelerate owing to the external force from the near-contact region. The centroid velocity keeps decreasing as more of the initial kinetic energy is transformed into deformation energy. The magnitude of the fluid motion keeps increasing too until at some point the centre of mass velocity, $U_{com} = 0$. However, the external force continues to act and the motion of the drops reverses. As the drops rebound, U_{com} increases until finally the drops rebound back to their initial positions. We note that (2.20) predicts that the velocity will be zero at a scaled time of 0.5 reflecting the symmetric nature of the collision process in the limit of zero Weber number. The effects of finite Weber number, however, render the collision process asymmetric and hence the actual time when U_{com} goes to zero is slightly different from 0.5 (for example, when $We_d = 10^{-3}$, the sign reversal happens at a dimensionless time of approximately 0.52). In addition, even when the collision is complete, the magnitude of the centre of mass velocity is less than 1, indicating that some of the initial energy is not recoverable. The same qualitative picture is obtained from a consideration of the kinetic energy associated with the fluid modes $E_{KE} = E'_{KE}(\rho_d a^3 U_c'^2)^{-1}$. The drops

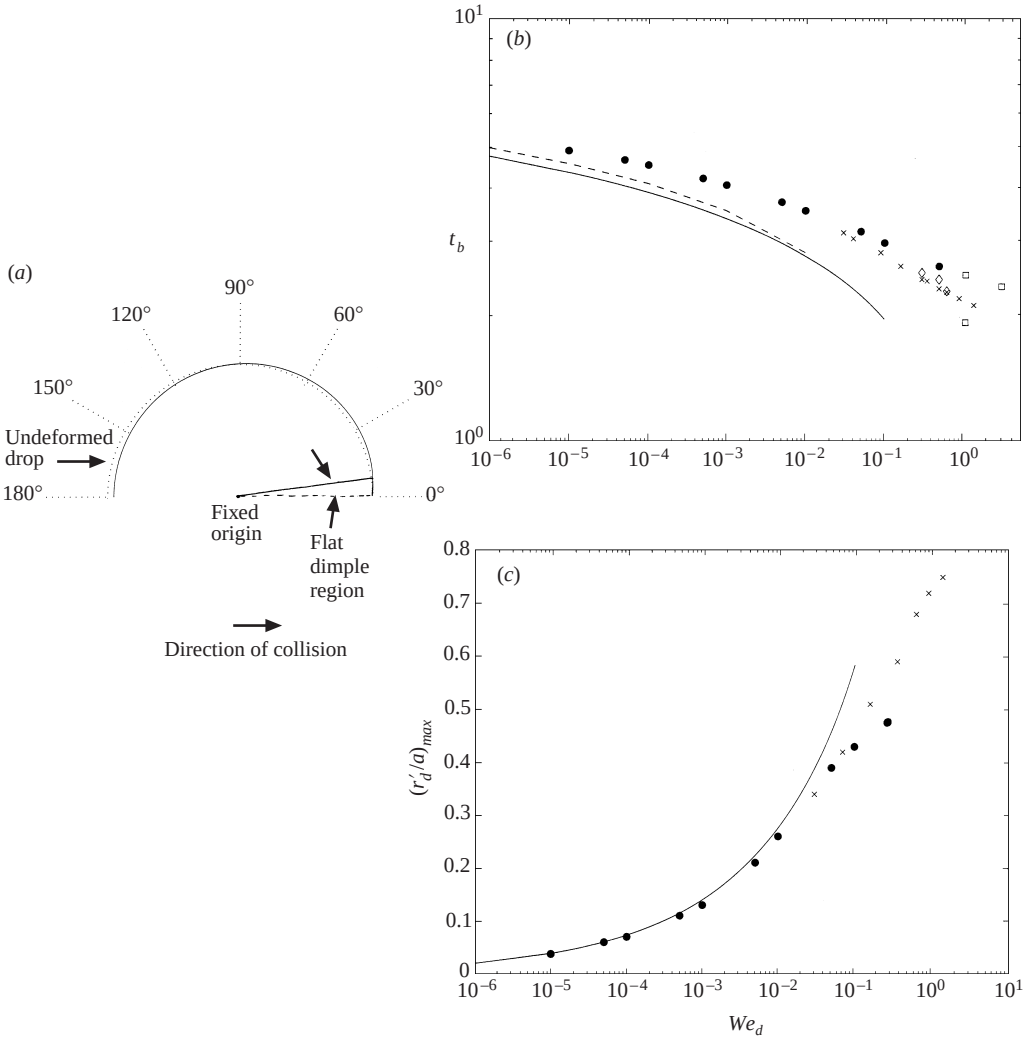

FIGURE 3. (*a*) The shape of drop 1 when the flat dimple region attains its maximum radial extent. The Weber number is 10^{-3}. The radial distances from the fixed origin (in drop 1) to the interface are scaled by *a*. The solid curve is the actual drop shape while the dashed curve represents the undeformed drop. Only half of the domain is shown since the shape is axisymmetric. (*b*) The scaled bounce time, t_b, as a function of the Weber number. ●, our numerical results; ×, Foote's simulation results. The dashed and the solid curves represent asymptotic expansions valid for small Weber number. ◇, results from experiments by Park (1970); □, experimental results from Jayaratne & Mason (1964). (*c*) Scaled maximum extent of the flat dimple region as a function of the Weber number, We_d. The solid line is the asymptotic expression valid when $\ln(We_d^{-1/4}) \gg 1$. ●, numerical results obtained from solving the equations in the previous section. ×, Foote's simulation values.

remain deformed and undergo shape oscillations even when they have rebounded back to their initial separations. Our results also show that the minimum values of the the kinetic energy and $|U_{com}|$ are attained at different times.

The main variables predicted from this potential flow analysis that can be compared to existing simulations by Foote (1975), and experiments by Jayaratne & Mason (1964) and Park (1970) are the time scales over which the drop bounce occurs (or equivalently the total time of apparent contact) and the maximum extent of the flat dimple region.

Figure 3(*b*) shows the dimensionless bounce time for the drop collision as a function of the Weber number. The filled circles are results of our numerical computations and the crosses are results from Foote's simulations. We see that the two are in very good agreement in the region where they overlap. Our analysis gives very good results up to Weber numbers of 0.2–0.3. The solid line is the asymptotic result given by

$$t_b = \pi\sqrt{\tfrac{2}{3}}\ln^{1/2}(We_d^{-1/4}), \tag{2.25}$$

and the dashed line is the improved asymptote obtained from equation (2.19). Our theory predicts a monotonic decrease in the scaled bounce time whereas experiments and exact simulations show that the bounce time reaches a minimum and then increases. The diamonds are Park's results for collision of two equal sized water droplets in air. We see that there is good agreement with our predictions for the bounce time in the range of moderately small Weber number of $O(0.1)$. The squares are Jayaratne & Mason's results for the rebound of a water droplet from a plane air–water interface.

Figure 3(*c*) is a plot of the scaled maximum extent of the flat dimple region, α_{max}, as a function of the Weber number. Again, the solid line is the asymptotic expression valid when $\ln(We_d^{-1/4}) \gg 1$:

$$\alpha_{max} = \left[\frac{2We_d}{3\ln(We_d^{-1/4})}\right]^{1/4} \tag{2.26}$$

and the filled circles are numerical results obtained from solving the equations in the previous section. The crosses represent Foote's simulation values. Excellent agreement is seen for values of the Weber number up to 0.2. As the Weber number goes to zero, the force required to cause the deformation decreases. The sum of the deformation modes of the drop surface is logarithmically larger than the mode due to translation: hence, the width of the dimple region decreases by a similar factor to keep the energy constant. This also means that the work done against the constant external pressure also decreases as more energy is stored as reversible surface energy. Thus, as the Weber number goes to zero, the scaled dimple extent goes to zero too.

An estimate of the net energy transferred to deformation modes at the end of the rebound process may be obtained by calculating the difference in the centre of mass velocity before and after collision (when D_1 equals zero). Figure 4 shows us the fractional loss in the centre of mass momentum, L of the drop as a function of the Weber number. As $We_d \to 0$, the value of L tends to zero too because the bouncing process becomes perfectly elastic A visual curve fit over Weber numbers in the range $O(10^{-4}$–$10^{-1})$ indicates that $L \sim 0.1We_d^{0.22}$. As the Weber number goes to zero (for values smaller than say 10^{-5}), L tends to zero faster than that predicted by this approximate curve fit. Karl & Frohn (2000) and Yao & Cai (1988) analysed published experimental data on bouncing of water and ethanol drops of radii 90–210 μm microns from heated walls above the Leidenfrost temperature. They concluded that the momentum loss in the collision was a weak function of Re_d for $We_d \leqslant 25$. This observation is consistent with Foote's simulation results that show that We_d plays a more important role than Re_d in the rebound process. The momentum loss, as determined by these investigators is given by the scaling law $L \sim 0.29We_d^{0.257}$ for $We_d \geqslant 1$ and is plotted as a dashed curve in the same figure. The increase in the exponent as the Weber number increases can be attributed to the following. We are neglecting viscous dissipation in the gas as well as in the drop,

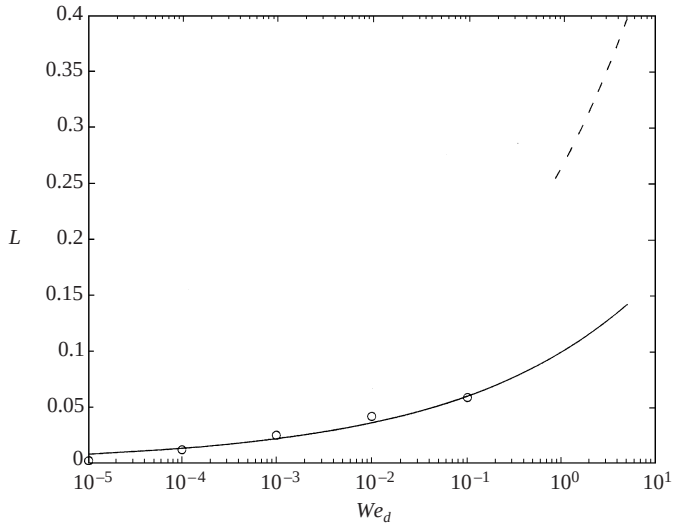

FIGURE 4. Momentum loss due to residual energy in deformation and fluid modes as a function of Weber number. ○, our numerical results; ——, the power law fit to our numerical results ($We_d^{1/2}/Re_d \to 0$); – – –, the fit to experimental data proposed by Karl & Frohn (2000).

and our scaling will be a lower bound on the actual energy loss. Furthermore, as the Weber number increases, more energy is channelled into surface oscillations owing to the large deformations that occur and hence the velocity of the centre of mass after rebound is likely to be less. Note that the approximate curve fit for large We_d completely neglects the dissipation in the gas film due to gas viscosity. Our model also does not take this into consideration, but it is likely that the experiments used to obtain the fit were affected by the gas.

Before concluding this section, we would like to briefly revisit equation (2.5) in light of the observations made regarding the propagation of surface disturbances on the drop surface. Equation (2.5) assumes a quasi-static response of the surface to the pressure. For small Weber numbers, we expect that the surface waves excited due to the localized force have time to propagate and move away before very short wavelengths and singularities in curvature can develop. For a freely oscillating drop in the absence of external forces, the frequency for the kth mode of oscillation ($k \geqslant 2$) is given by the equation $\omega^2(k) = k(k-1)(k+2)\sigma(\rho_d a^3)^{-1}$. The slowest oscillatory mode (with the smallest frequency) is the $k = 2$ mode. Even, as in the case we have just studied, when surface oscillations are excited by localized forces, the leading (and slowest) mode of oscillation is the $k = 2$ for which the frequency is given by $\omega_{min} = (8\sigma/\rho_d a^3)^{1/2}$.

2.4. *First effects of drop viscosity* – $We_d^{1/2}/Re_d \ll 1$

In the potential flow analysis, viscous effects in the drop are neglected and hence there is no dissipative mechanism to dampen surface oscillations and velocity fluctuations due to the collision. In actual collisions, even though viscous effects might not be very important during the short time the drops are in near-contact, they will eventually become important as the drops move away.

2.4.1. *Viscous dissipation due to the primary, inviscid flow*

An estimate of the rate of viscous dissipation due to the primary potential flow may be made easily. Analysis indicates that the rate of energy dissipated due to viscosity in the drop is given by:

$$\Pi_{vis} = \left[-\mu_d \int_{\mathscr{V}_{drop}} (\nabla' \boldsymbol{u}'_d : \nabla' \boldsymbol{u}'_d) \mathrm{d}\mathscr{V}'\right] = -\frac{U_c'^3 \rho_d a^2}{Re_d} \varpi, \tag{2.27}$$

where,

$$\varpi = 2\pi \int_0^{\pi} \sin\theta \, \mathrm{d}\theta \int_0^1 (\nabla \boldsymbol{u}_d : \nabla \boldsymbol{u}_d) r^2 \, \mathrm{d}r + 2\pi We_d^{1/2} \int_0^{\pi} \sin\theta \, \mathrm{d}\theta \int_0^{\mathscr{H}(\eta,t)} (\nabla \boldsymbol{u}_d : \nabla \boldsymbol{u}_d) \, \mathrm{d}y,$$

where $y = (r-1) We_d^{-1/2}$. The expressions for $\boldsymbol{u}_d$ and the drop deformation in the above equation are as given by (2.3) and (2.6). A simple scaling argument indicates that the net viscous dissipation over the bounce time is roughly $O(\rho_d U_c'^2 a^3 We_d^{1/2} Re_d^{-1})$. A more exact analysis using equation (2.27) and the properties of Legendre polynomials indicates that in the limit $\ln(We_d^{-1/4}) \gg 1$, $\varpi \sim O(\ln^{-2}(We_d^{-1/4}))$.

2.4.2. *First effects of drop viscosity on rebound process when* $We_d^{1/2} \ll Re_d$

The first effects of drop viscosity for small values of $We_d^{1/2}/Re_d$ may be incorporated into the potential flow analysis done in the previous section by including a dissipative force in the momentum equation for the fluid modes. Consider the rate at which the total energy contained in the fluid modes is dissipated by drop viscosity. Owing to the linear nature of the governing equations, the viscous dissipation for each mode k can be calculated independently of other modes. The balance for each mode is given by:

$$\rho_d U_c'^3 a^2 We_d^{-1/2} \left(\frac{\mathrm{d}B_k}{\mathrm{d}t}\right)_{vis} = -\mu_d a U_c'^2 (k-1)(2k+1) B_k, \tag{2.28}$$

where the subscript *vis* indicates that this balance does not take into account the energy generated due to the force in the inner flat region. (Physically, this equation is obtained by analysis of the total kinetic energy of the drop associated with the velocity modes B_k. The effects of viscous dissipation are represented via a fictitious force that leads to a decrease in the total kinetic energy of the fluid motions in the drop.) The modified rate at which the velocity modes change due to inclusion of viscous effects can now be obtained by incorporating this energy loss term into equation (2.10) to get,

$$\frac{\mathrm{d}B_k}{\mathrm{d}t} = -We_d^{-1/2}[\mathscr{P}_{k-1}(\cos\alpha) - \mathscr{P}_{k+1}(\cos\alpha)] - [k(k+1)-2]D_k - \frac{We_d^{1/2}}{Re_d}(k-1)(2k+1)B_k. \tag{2.29}$$

We note that this scaling for the energy loss is consistent with the $O(We_d^{1/2}/Re_d)$ term we neglected in the Navier–Stokes equation. Thus, we find that higher-order modes, which also have higher frequencies and smaller amplitudes, are dissipated faster. In fact, equation (2.29) indicates that the amplitude B_k of the kth mode in the absence of any energy inputs would decrease exponentially over a time scale $O[(k-1)^{-1}(2k+1)^{-1} Re_d a U_c'^{-1}]$. Clearly, even for the $k = 2$ mode, viscous decay occurs over a time scale that is $O(We_d^{-1/2} Re_d^{-1})$ larger than the time over which the bounce occurs.

In obtaining equations (2.28) and (2.29), we assumed that the governing equations for the fluid velocity were linear. Thus, the analysis is strictly applicable when the viscous effect acts as a small perturbation to the inviscid base state, i.e. $We_d^{1/2}/Re_d \ll 1$ and the viscous term is more important than the nonlinear term. Of course, in most cases of interest (as shown in table 1), the Reynolds number is in the range $O(0.1) - O(10)$ so this simple analysis is expected to give a reasonably qualitative picture of the effects of drop viscosity. It is interesting, however, to note that nonlinear inertial effects are predicted to be more important than viscous effects for moderate and large Reynolds numbers. This is indeed observed to be the case in experiments and also in Foote's simulations where the dynamics of the rebound was found to be relatively insensitive to the drop Reynolds number.

Figure 5(a) shows the centre of mass velocity B_1 as a function of dimensionless time for $Re_d = 0.5, 2$ and 20 and a Weber number of 10^{-2}. As the Reynolds number decreases, more of the initial kinetic energy is dissipated and hence the drop speed when the rebound process ends follows a decreasing trend. The rebound times increase with decreasing Re_d. This is likely to be due to the decrease in the centre of mass velocity compared to the truly inviscid case. However, the magnitude of the change is very small for the range of Reynolds numbers considered. At $t = 0$, the distance between the drops' centroids is $2a$. As the collision progresses this distance decreases, indicating that if the drops were rigid spheres, they would overlap, i.e. the distance between their centres of mass would be less than $2a$. We define the magnitude of the difference between the centroid to centroid distance and $2a$ as the overlap thickness. Figure 5(b) shows plots of the rebound time (solid line) and the maximum overlap thickness (dashed line), as functions of Re_d for $We_d = 10^{-2}$. Both the rebound times and the overlap thickness are normalized with the corresponding values obtained in the limit $Re_d \to \infty$. We find that the degree of maximum overlap decreases slightly as the Reynolds number decreases. This may be attributed due to increasing viscous dissipation leading to a reduction in the energy available to overcome the force resisting the relative approach of the drops. As mentioned before, the bounce time increases as viscous effects become more important owing to the decrease in the centre of mass velocity. As Re_d decreases, dissipation becomes important. Consequently, the net energy available to do work against the constant pressure also decreases.

Consider now the temporal evolution of $\alpha(t)$ when drop viscosity is neglected. The higher-order deformation modes $k \gg 1$ are comprised of a quasi-steady part that is in equilibrium with the applied force and a smaller, high-frequency component that has a small $O(2\pi/k^{3/2})$ period. Owing to the coupling between the deformation modes and the extent of the dimple, as reflected in equation (2.7), these surface fluctuations cause oscillations in α too. For extremely small values of the Weber number (say, 10^{-5}), the modes that control the dimple area are the $k = 1$ and $k \gg 1$ modes. Thus the magnitude of the oscillations in α for $We_d = 10^{-5}$ are smaller and have a higher frequency. For the relatively larger Weber number of 10^{-3}, the area of the dimple region is controlled by modes that are $O(10)$ and so the time scale for the bounce is comparable to the time scale characterizing the oscillatory behaviour of these modes. A clearer picture of dissipative effects of drop viscosity on the deformation is seen in figure 6 which shows the temporal evolution of the radial extent of the dimple as a function of time for a Weber number, $We_d = 10^{-2}$. The higher-order deformation modes oscillate with smaller amplitude and larger frequency. When viscosity is introduced, the dissipative mechanism causes a dampening of the oscillations. Equations (2.28) and (2.29) indicate that one may expect rapid suppression of the large-frequency, small-amplitude oscillations. The smoothing effect increases as the Reynolds number decreases, as is expected.

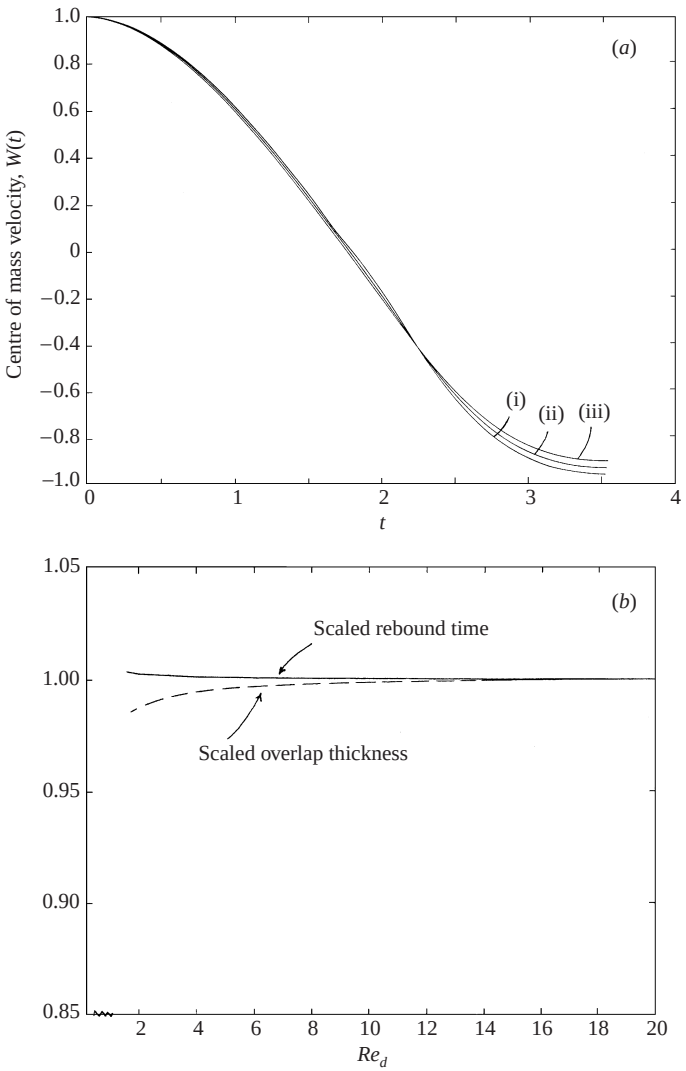

FIGURE 5. First effects of viscous dissipation for $We_d = 10^{-2}$: (*a*) the temporal evolution of the centre of mass velocity for $Re_d = 0.5, 2$ and 20 (denoted by numbers 3, 2 and 1, respectively); (*b*) the normalized rebound times and the maximum overlap thickness as functions of Re_d.

3. Effects of flow and viscous dissipation in the gas film on the collision dynamics

In the previous section, we neglected flow and thus viscous dissipation in the gas film separating the drops. Furthermore, we assumed that the thickness of the thin film did not change much in the time over which the rebound occurred. In this section, we use matched asymptotic techniques to obtain the equations governing the evolution of the gap between the drops and the deformation of the drop interfaces. The inner region in the vicinity of near contact is analysed first. We show that in order to complete the formulation, the flow and deformation in the entire drop has to be evaluated. Using a matching technique valid in the limit $\ln(We_d^{-1/4}) > 1$, we obtain the complete set of equations which are then solved numerically to obtain a detailed

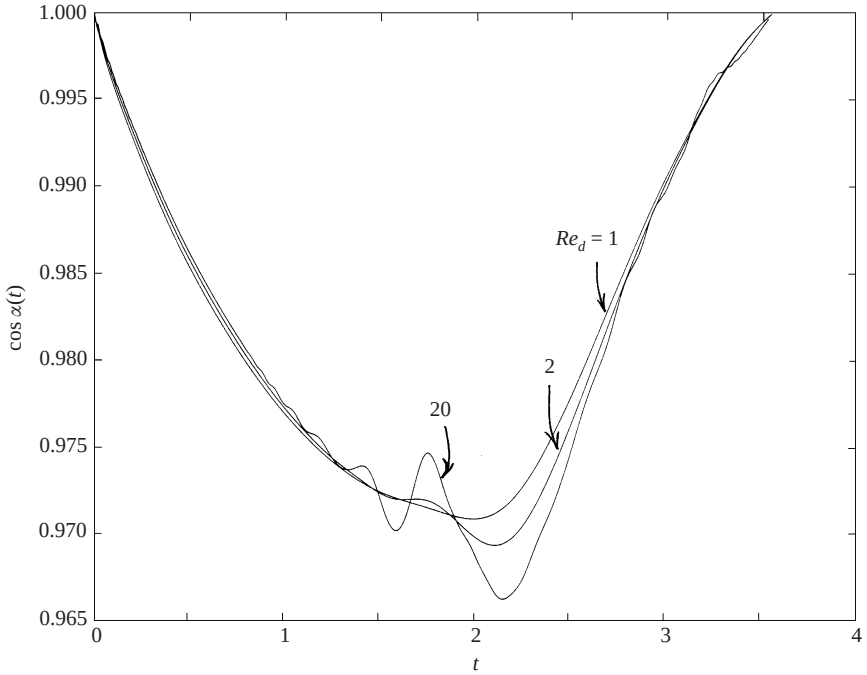

FIGURE 6. Effect of increasing viscous dissipation on the oscillations in $\alpha(t)$. The Weber number, We_d, is 10^{-2} and the Reynolds numbers, Re_d are 1(the smoothest curve), 2 and 20 (curve with pronounced oscillations), respectively.

description of the approach and rebound process. The results we obtain also allow us to test the validity of the assumptions made in § 2.

3.1. *Outer trajectory analysis*

A proper transition should be made from the solution for the outer trajectory starting from separations of $O(a)$ where lubrication effects are not present to the solutions of the thin film lubrication equations at close contact. In order to initiate these lubrication calculations, we need asymptotically correct initial deformation and rate of deformation values that take into account deformation prior to the establishment of the lubrication flow. We can show, using a scaling analysis, that when $Ca_g^{1/2} \ll 1$, the initial deformation is $O(aCa_g)$. Since the deformation during the rebound process is $O(aWe_d^{1/2})$, the asymptotically correct initial conditions are thus zero initial deformation. It can also be shown that the rates of deformation are zero to leading order. More details can be found in Appendix A.

3.2. *Analysis of close contact motion*

3.2.1. *Analysis of the inner lubrication region*

The geometry and orientation of the two-sphere head-on collision is as shown in figure 1. At small separations, $h' \ll a$ the flow of the gas in the small intervening gap is viscous and almost unidirectional. The motion of two spherical drops of radii a separated by a distance h' and moving with a relative speed $2U_c'$ induces a pressure in the gap that is $O(\mu_g U_c' a/h'^2)$ if $h' U_c' \rho_g \mu_g^{-1} \ll 1$ and the gas is incompressible and a continuum in nature. Significant deformation of the interface occurs when

this lubrication pressure balances the capillary pressure $2\sigma/a$. For an incompressible, continuum gas, the characteristic gap width, l, at which deformation becomes important is thus $l \equiv aCa_g^{1/2}$. Note that since $Ca_g \ll 1$, deformation effects become important only when the gap is small enough that a lubrication type analysis applies. Furthermore, we find that the Reynolds number based on l is much less than one, so that the flow of the gas is governed by the Stokes equations. Since we are interested in effects of deformation, we choose l as our characteristic axial length scale. The characteristic radial length scale in the region of close contact is taken to be $(al)^{1/2}$. We choose the initial velocity U_o' when the lubrication calculations are started as our characteristic axial velocity scale. Since $St > 1$, this choice allows us to relate our theoretical predictions with simulation and experimental results that are formulated in terms of the velocity prior to the collision process. Velocities in the radial direction are scaled by $U_c'(a/l)^{1/2}$. As the drops come closer, the surfaces deform and this process leads to energy being stored as deformation energy. For large Stokes numbers, it is reasonable to expect that the energy stored in the deformation modes will be of the order of the initial kinetic energy of the drop, $O(\rho_d U_c'^2 a^3) = O(a^2\sigma We_d)$. Thus, the surface of the drop is expected to deform by an $O(aWe_d^{1/2})$ amount, and we choose to scale the deformation with this length scale. The time scale of the collision process is very small and the characteristic acceleration of the centre of mass of each drop will be $O(U_c'^2 We_d^{-1/2} a^{-1})$, and much greater than the acceleration due to gravity and so gravity effects on the total force can be ignored for most of the collision. For strongly or moderately bouncing drops, the collision and bounce time is expected to be approximately the time it takes for the centre of mass of the drop to travel a vertical distance of the order of the deformation, and so we choose $aWe_d^{1/2}U_c'^{-1}$ as a characteristic time. The characteristic pressure, p_c, used in the scalings is σ/a.

The drop surface can be considered tangentially immobile for calculating the gas flow field, if the tangential velocity of the fluid inside the drop induced due to radial motion of the gas in the gap is small compared to the radial gas velocity. If the gap thickness at any instant in time is h', the characteristic size of the region inside the drop (in the lubrication region) over which gradients of flow and pressure occur is $O([ah']^{1/2})$. When $h' \sim O(a\mu_g^2\mu_d^{-2})$, the radial flow of the gas will cause the interface to move tangentially with velocity of the order of the radial gas velocity. For gap thicknesses larger than this, the drop surfaces are tangentially immobile to leading order (Davis, Schonberg & Rallision 1989). Once strong deformation sets in, the characteristic spatial extent in the lubrication region over which large gradients in the drop exist is $O(aWe_d^{1/4})$ for $St \gg 1$. However, the minimum gap width will still be $O(aCa_g^{1/2})$, and so as long as $Ca_g \gg (\mu_g/\mu_d)^4$, the drop interfaces can be considered tangentially immobile insofar as the gas flow in the thin film is considered. For water droplets in air, the viscosity contrast μ_d/μ_g is about 100. Taking $aCa_g^{1/2}$ as the characteristic gap thickness we find that for capillary numbers of $O(10^{-3}$–$10^{-6})$ the criterion derived above is satisfied. We note that at gap separations of $O(aCa_g^{1/2})$, the deformation-induced drop pressure in the lubrication region is $O(\rho_d U_c'^2 Ca_g^{1/4})$. The pressure generated by the viscous term due to the induced tangential velocity is $O(\mu_d U_c' Ca_g^{-1/4}/a)$. Both these terms are much smaller than the pressure in the gas that is of $O(\sigma/a)$ if $We_d^{3/4} \ll 1$ and $Ca_g^{3/4} \ll 1$. For $Ca_g^{1/2}\mu_d/\mu_g = O(1)$, the tangential velocity at $h' = O(aCa^{1/2})$ is of the order of U_c'. For smaller capillary numbers, the tangential interface velocity is $O(U_c')$ at separations larger than $O(aCa_g^{1/2})$. Even then, as far as the gas is concerned, the $O(U_c')$ tangential velocity is still a factor $Ca_g^{1/4}$ smaller than the mean radial velocity of the gas and hence in order to calculate the

velocity field and pressure in the gap, we can assume zero tangential velocity at the surface.

We will show later on that the flow inside the drop is potential flow, the viscous terms being negligible for $Re_d \gg We_d^{1/2}$. In most cases, $Re_d \gg 1$, so that viscous effects are confined to a thin boundary layer near the surface of the drop where the tangential velocity adjusts from the value obtained based on the solution of the gas flow to the value given by the potential flow solution. The gas flow in the outer region may be neglected to leading order, and so the tangential velocity of the interface induced by the outer gas flow is small. In the $O(aWe_d^{1/2}U_c'^{-1})$ time it takes for the collision to occur, the boundary layer that develops in the lubrication region, penetrates into the drop to an extent given by $a(Ca_g/St)^{1/4}(\mu_d/\mu_g)^{1/2}$. The boundary layer is confined to the lubrication region as long as the Stokes number, $St^{1/4} \gg (Ca_g^{1/2}\mu_d\mu_g^{-1})^{1/2}$. The normal interface stress resulting from this boundary layer is small compared with the flow induced drop pressure. Thus, as far as the flow inside the drop in the outer region is considered, we may model the interface as a stress-free, mobile interface.

We do not include any inter-particle attractive forces and also assume that there are no surfactants on the interfaces that give rise to surface tension gradients or repulsive forces. In addition, we also neglect the absorption of gas by the drop. Using Henry's law, we can estimate the fractional amount of gas in the gap that is absorbed during the collision process as $O(D_g c_s t_c'(ah'c_g)^{-1})$ and this is typically of the order of 10^{-5} or so. Here, D_g is the gas diffusion coefficient, c_s is the molar concentration of the gas on the surface, c is the molar concentration of the gas in the gap, h' is a typical gap width during the collision process that lasts for a time t_c'.

In the near contact region (see figure 1*b*), the two undeformed spheres can be approximated by paraboloids. The gap extends in the z-direction from H_1' to $H_2' = -H_1'$, where,

$$H_1' = -\tfrac{1}{2}H' = -\left(h' + \frac{1}{2}\frac{r'^2}{a} + D'\right), \tag{3.1}$$

D' being the deformation in the z-direction measured as indicated in the figure. The centres of mass of the spheres move towards one another with speeds U_1' and U_2', where, $-U_1' = U_2' = W'$. The flow of the gas in the gap when the gas behaves as a continuum incompressible fluid is governed by the continuity equation which in scaled form reads:

$$\frac{1}{r}\frac{\partial}{\partial r}(ru_r) + \frac{\partial u_z}{\partial z} = 0. \tag{3.2}$$

The rate at which the centre of mass of drop 2 moves is given by:

$$\left(\frac{Ca_g}{We_d}\right)^{1/2}\frac{\mathrm{d}h}{\mathrm{d}t} = W. \tag{3.3}$$

In the lubrication region, the unit normals to the two surfaces are in the z-direction (to leading order) and, hence, we can write expressions for the rates at which the interfaces move:

$$\left(\frac{Ca_g}{We_d}\right)^{1/2}\frac{\partial H_1}{\partial t} = u_z(H_1), \quad \left(\frac{Ca_g}{We_d}\right)^{1/2}\frac{\partial H_2}{\partial t} = u_z(H_2). \tag{3.4}$$

To obtain an equation for the pressure in the gap, we integrate the scaled continuity

equation over the inter-sphere gap and use equations (3.3) and (3.4):

$$\frac{1}{r}\frac{\partial}{\partial r}(rj) + 2W + 2\frac{\partial D}{\partial t} = 0. \tag{3.5}$$

Here, j is the dimensionless fluid flux per unit circumference out of the gap and is defined as:

$$j = \int_{H_1}^{H_2} u_r \, \mathrm{d}z. \tag{3.6}$$

To obtain an equation for the flux, we must scale the momentum equations and consider the relative magnitude of the different terms. Since $Re_l \equiv (a\mu_g^{-1}U_c'\rho_g Ca_g^{1/2}) \ll 1$ and typical values of $Re_l(Ca_g/We_d)^{1/2}$ are very small, the equation for the radial pressure gradient reduces to a simple form:

$$-\frac{\partial p_g}{\partial r} + \frac{\partial^2 u_r}{\partial z^2} = 0.$$

In the limit of small $Re_l \ll 1$ and for weakly deforming drops, the pressure gradient along the gap develops owing to radial motion of the gas out of the gap. Scale arguments indicate that $\partial p_g'/\partial z'$, is small compared to radial variations in the pressure. Using this, the momentum equations can be solved for the radial velocity of the gas. We obtain,

$$u_r = \frac{1}{12}\frac{\partial p_g}{\partial r}[z^2 - (H_1 + H_2)z + H_1H_2].$$

From this, we can obtain the following expression for the flux valid for continuum flow:

$$j = -\frac{H^3}{12}\frac{\partial p_g}{\partial r}. \tag{3.7}$$

The pressure field satisfies $(\partial p_g/\partial r)_{r=0} = 0$ and $p_g \to p_\infty$ for $\max[1, (We_d/Ca_g)^{1/4}] \ll r$. For very large values of the Stokes number, the characteristic radial extent of the lubrication region scales as $aWe_d^{1/4}$. In deriving these governing equations, we have used $aCa_g^{1/4}$ as the radial scale. An overall force balance on the drop is obtained by integrating the pressure over the drop surface and this force determines the rate at which the velocity of the centre of mass changes:

$$\frac{\mathrm{d}W}{\mathrm{d}t} = \frac{3}{2}\left(\frac{Ca_g}{We_d}\right)^{1/2}\int_0^{r_\infty}(p_g - p_\infty)r \, \mathrm{d}r. \tag{3.8}$$

The shape of the air–drop interface is determined by the balance between the exterior (gas) and interior (drop) pressures at the interface and the capillary pressure which is a consequence of the finite interfacial tension and the curvature of the interface. The stress balance at interface S_i of drop i may be written in the form:

$$p_{d,i}' - p_g' - 2\mu_g(\boldsymbol{n}_i \cdot \boldsymbol{e}' \cdot \boldsymbol{n}_i) + 2\mu_d(\boldsymbol{n}_i \cdot \boldsymbol{E}_i' \cdot \boldsymbol{n}_i) = \pm\sigma(\nabla' \cdot \boldsymbol{n}_i), \tag{3.9}$$

p_d' is the dimensional drop pressure, while $\boldsymbol{e}'$ and $\boldsymbol{E}'$ represent the traceless, symmetric parts of the viscous stress tensor in the gas and in the drop, respectively. The unit normals $\pm\boldsymbol{n}$ are chosen such that the pressure inside each non-deformed drop is greater than that outside by the quantity $2\sigma/a$. Equation (3.9) is valid at all points on the drop surfaces. In the inner region, however, the two interfaces are nearly planar and parallel to the $z = 0$ plane and this permits considerable simplification. The

following equation for the deformation of the surface of drop 2 is easily obtained:

$$\frac{1}{r}\frac{\partial}{\partial r}\left(r\frac{\partial D}{\partial r}\right) = \left(\frac{Ca_g}{We_d}\right)^{1/2}\left[p_\infty - p_g + a\frac{p'_{d,c}}{\sigma}P_s\right], \tag{3.10}$$

where, the drop pressure at the interface $(p'_d)_s$ has been written as $p'_o + 2\sigma/a + p'_{d,c}P_s$. In equation (3.10), $p'_{d,c}$ is a characteristic fluid pressure induced due to the drop motion and P_s is the dynamic drop pressure evaluated at the interface. For $St > 1$, the radial extent of the region inside the drop where strong flow gradients are induced is $O(aWe_d^{1/4})$. Since the collision takes place on a time scale $O(aWe_d^{1/2}/U'_c)$, the characteristic pressure $p'_{d,c}$ in the inner region is $O(\rho_d U_c'^2 We_d^{-1/4})$. In order to be able to neglect P_s, we want $p'_{d,c} \ll 2\sigma/a$. This criterion gives the condition, $We_d^{3/4} \ll 1$. Thus, we find that the deformation in the lubrication region is determined by a balance between the gas pressure in the gap and surface tension forces. In any case, viscous pressure gradients in the drop due to deformation-induced flow in the gap can be neglected if $\mu_d\mu_g^{-1}Ca_g < 1$.

Multiplying (3.10) by r and integrating over r using the symmetry condition $\partial D/\partial r = 0$ at $r = 0$ we obtain:

$$r\frac{\partial D}{\partial r} = -\frac{2}{3}\frac{\mathrm{d}W}{\mathrm{d}t} - \left(\frac{Ca_g}{We_d}\right)^{1/2}\left[\int_r^{r_\infty}(p_\infty - p_g)r^*\,\mathrm{d}r^*\right]. \tag{3.11}$$

Thus, we obtain the following asymptotic behaviour of $D(r,t)$ as $r \to r_\infty$:

$$D(r) \approx -\frac{2}{3}\frac{\mathrm{d}W}{\mathrm{d}t}\ln r + f(t) + O\left(\left(\frac{Ca_g}{We_d}\right)^{1/2}\frac{\ln r}{r^2}\right). \tag{3.12}$$

In the limit $\max[Ca_g, We_d] \ll 1$, we may replace r_∞ in the above equations by infinity without loss of generality. The logarithmic divergence of the deformation indicates that the entire drop deforms and not just the near-contact regions. This may be contrasted with inertia driven elastohydrodynamic collisions between deformable solid spheres where the deformation is confined only to the lubrication region and hence analysis of the near-contact region alone provides a description of the collision dynamics. Our analysis shows that for deformable drops undergoing a collision, such a local analysis is not sufficient and the deformation of the entire drop has to be considered. However, drop–drop collisions are similar to buoyancy driven collisions of a deformable drop with a rigid or deformable air–water interface. In the latter case, the deformation of the drop and the interface are of the same order. The time scale for the drop bounce is determined by the rate at which the deformation throughout the drop relaxes. Thus, the flow and deformation in the inner region is fully coupled to the flow inside the drop. The divergence of the deformation contrasts with the asymptotic behaviour of the gas pressure for very large values of r which is as follows:

$$p_g - p_\infty \approx 2\frac{\mathrm{d}^2W}{\mathrm{d}t^2}\frac{\ln r}{r^4} - \left(\frac{1}{2}\frac{\mathrm{d}^2W}{\mathrm{d}t^2} + 3W + 3\frac{\mathrm{d}f}{\mathrm{d}t}\right)\frac{1}{r^4}. \tag{3.13}$$

3.2.2. *Outer problem for the drop deformation*

When $r' \gg r'_\infty$, the pressure p'_g is approximately equal to the bulk value p'_∞. Consequently, when the curvature of the interface becomes important, the gas pressure has nearly decayed to its bulk value and we expect the extent of deformation to be determined by a balance between the surface tension (capillary) pressure and the

pressure induced inside the drop owing to the flow set up by the deformation in the lubrication region. This balance will occur if the characteristic dynamic pressure in the drop is much greater than the characteristic gas pressure outside the drop. Far from the lubrication region, we expect the characteristic gas pressure to scale like $O(\mu_g U_c'/a)$ and we will find later that the dynamic pressure in the drop scales like $O(\rho_d U_c'^2 We_d^{-1/2})$. So, as long as $Ca_g \ll We_d^{1/2}$, the effects of gas flow in the outer region can be neglected. As seen from the outer region, the inner lubrication region shrinks to a point. All details of the pressure profile are lost and the only relevant information that is transmitted to the outer region is some sort of averaged information. These observations motivate a simpler treatment of the deformation in the outer region.

It is convenient to use a coordinate system that readily allows us to decouple the gap thickness from the drop deformation. So we now choose a new spherical coordinate system (r^*, θ, ϕ) with origin at the centre of mass of drop 2, as shown in figure 1(*a*). This origin, $\boldsymbol{O}_2$, is thus accelerating in a reference frame that is fixed at $\boldsymbol{O}_1$ as shown in figure 1. The spherical coordinate system has its polar axis oriented in the direction of the acceleration (line of centres) so that the fluid velocity and droplet deformation in either reference frame is symmetric with respect to the polar axis i.e. $\partial(.)/\partial\phi = 0$. The droplet surface is at all times during the collision process assumed to be slightly perturbed from its equilibrium value $R' = a$.

As seen in the accelerating reference frame, there exists a static pressure gradient in the gas and in the drop that results from the pseudo-force needed to keep the centre of mass stationary. We retain this force in the momentum balance for the liquid in the drop since it is of the same order as the leading order inertia terms. In the gas, this induces a pressure that is at most $O(\rho_g a U_c'^2 We_d^{-1/2})$ on the surface of the drop and this may be neglected compared to the much larger $O(\rho_d a U_c'^2 We_d^{-1/2})$ dynamic pressure induced in the drop. In addition, this $O(\rho_g a U_c'^2 We_d^{-1/2})$ pressure term is smaller than the $O(\sigma/a)$ pressure that develops in the lubrication region during the bouncing process. Consequently, the gas pressure in this non-inertial frame is the same as that in the stationary reference frame to leading order.

Let the centre of mass undergo an acceleration

$$\boldsymbol{A}'_{com}(t') = \frac{\mathrm{d}W'}{\mathrm{d}t'}\boldsymbol{e}_z$$

at any instant in time t', $\boldsymbol{e}_z$ being the unit vector in the z'-direction along the line of centres. In the accelerating reference frame, the flow inside the drop is governed by the Navier–Stokes equations with a term to account for the pseudo-force due to the acceleration. Since we are interested in spatial length scales of $O(a)$ (far from the lubrication region), we scale all spatial gradients by $1/a$. Fluid velocity $\boldsymbol{u}'_d$ is scaled with U_c' and time t' is scaled by $aWe_d{}^{1/2}/U_c'$. The scaled Navier–Stokes equation then reads:

$$\frac{\partial \boldsymbol{u}_d}{\partial t} + We_d^{1/2}\boldsymbol{u}_d \cdot \nabla \boldsymbol{u}_d + \frac{p'_{d,c}}{a}\nabla P = \frac{We_d^{1/2}}{Re_d}\Delta \boldsymbol{u}_d + \frac{We_d^{1/2}}{Fr_d}\frac{\boldsymbol{g}}{g} - \frac{aA'_{com}We_d^{1/2}}{U_c'^2}\boldsymbol{e}_z. \qquad (3.14)$$

As in § 2, we consider drops for which $We_d^{1/2} \ll 1$, $Fr_d = U_c'^2/ag \gg 1$ and $We_d^{1/2}/Re_d \equiv \mu_d/(\rho'_d a\sigma)^{1/2} \ll 1$. The large Froude number limit implies that gravity effects may be neglected during the collision process. An examination of the scalings shows that

$$A'_{com} = \left(\frac{U_c'^2}{aWe_d^{1/2}}\right)\frac{\mathrm{d}W}{\mathrm{d}t},$$

and hence the centre of mass acceleration term is also $O(1)$, like the inertia term. Balancing the pressure gradients with inertia gives us the following scaling for the dynamic pressure, $p'_{d,c} \sim O(\rho_d U_c'^2 We_d^{1/2})$. The approximate form of the equation of motion during the collision process attains the form,

$$\frac{\partial \boldsymbol{u}_d}{\partial t} = -\nabla p_d = -\nabla P - \frac{\mathrm{d}W}{\mathrm{d}t}\boldsymbol{e}_z, \tag{3.15}$$

and is similar to equation (2.2). Here, P is the dynamic pressure satisfying the condition $P \to 0$ as $\boldsymbol{u}_d \to \boldsymbol{0}$. This equation represents the impulsive motion of the fluid in the short duration of the collision process.

Let the surface of the drop as measured from the centre of mass of the drop be given by

$$r_s^* = a(1 + We_d^{1/2}\mathscr{D}), \quad \mathscr{D}(\theta, t) = \sum_{k=0}^{\infty} \mathscr{L}_k(t)\mathscr{P}_k(\cos\theta). \tag{3.16}$$

The $k = 0$ mode corresponds to a volumetric pulsation whereas the $k = 1$ mode corresponds to the motion of the centre of mass relative to the centre of the coordinate system. Imposing the constraint of constant drop volume due to the incompressibility of the fluid and also the condition that the centre of mass lies at the origin of the coordinate system, we find both $\mathscr{L}_o$ and $\mathscr{L}_1$ to be zero for all time. The relative errors incurred while imposing the constant volume and centre of mass conditions are $O(We_d)$ and are small compared to the terms retained. Note that the volume of the inner dimple region is $O(We_d)$ and thus details of the dimple shape can be neglected in imposing the constant volume constraint. Since vorticity effects may be neglected and the fluid is incompressible, the velocity may be written as the gradient of a velocity potential that satisfies Laplace's equation in the interior of the drop,

$$\boldsymbol{u}_d = \nabla\phi, \quad \Delta\phi = 0. \tag{3.17}$$

Equation (3.17) presupposes that the potential at the origin (the inner region) is bounded and there is no source of mass/momentum to leading order. A local analysis of the liquid flow in the inner lubrication region shows that this is indeed the case. The characteristic length scale in this region is $O(aWe_d^{1/4})$ and the characteristic velocities are $O(U_c')$. Viscous effects can be neglected compared to inertial effects and so the characteristic pressure is $O(\rho_d U_c'^2 We_d^{-1/4})$, a factor $O(We_d^{1/4})$ smaller than the characteristic pressure in the outer region. The pressure gradients, however, have the same magnitudes as expected. The characteristic velocity potential in the inner region is thus $O(aU_c' We_d^{1/4})$, also a factor $O(We_d^{1/4})$ smaller than the value in the outer region. Thus, the velocity potential in the inner lubrication region is small and bounded. This implies that there cannot be a source term on the right-hand side of the Laplace equation for ϕ, namely, equation (3.17), since such a source term would imply that ϕ is singular at some point inside the drop region. In addition, we note that since ϕ has to be bounded, we can choose to express both $\mathscr{D}$ and ϕ as a linear superposition of any complete set of basis functions. We choose the Legendre polynomials as our basis functions for convenience.

The governing equations (3.15) and (3.17) are similar to that obtained previously for the idealized bounce problem in § 2. We now write the solution to (3.17) in a form similar to (2.8),

$$\phi = \sum_{k=0}^{\infty} B_k(t)(r^*)^k \mathscr{P}_k(\cos\theta). \tag{3.18}$$

Here, r^* is the scaled radial position as measured from the centre of mass and θ is the angular position as measured in this new coordinate system. Clearly, both B_o and B_1 are zero, owing to the choice of our reference frame.

The dynamic pressure inside the drop can now be written as:

$$P = -\frac{\partial \phi}{\partial t} + \frac{\mathrm{d}W}{\mathrm{d}t} r \cos\theta,$$

with the rate of change of velocity given by (3.8). Incorporating the expansions for the deformation and velocity potential in the kinematic interface condition, (2.4), we obtain the following equations relating the two sets of coefficients:

$$\frac{\mathrm{d}\mathscr{L}_k}{\mathrm{d}t} = kB_k, \quad k \geqslant 2. \tag{3.19}$$

Here, we used the fact that $\boldsymbol{U}_s$ is the velocity of the fluid relative to the centre of mass velocity evaluated at the particle surface.

The formulation of the problem, as stated above, allows us to obtain another relationship between the pressure inside the drop and the external pressure acting on the drop. By Newton's law we can write,

$$\begin{aligned} \mathscr{M}\boldsymbol{A}'_{com}(t') = \mathscr{M}A'_{com}(t')\boldsymbol{e}_z &= -\int_{\mathscr{A}_d} (p'_g - p'_\infty)\boldsymbol{n}_s \,\mathrm{d}\mathscr{A}_d \\ &= -\int_{\mathscr{A}_d} (p'_g - p'_\infty)(\boldsymbol{n}_s \cdot \boldsymbol{e}_z)\boldsymbol{e}_z \,\mathrm{d}\mathscr{A}_d, \end{aligned} \tag{3.20}$$

where $\boldsymbol{n}_s$ is the outward unit normal at a differential surface area $\mathrm{d}\mathscr{A}_d$ of the drop surface, $\boldsymbol{e}_z$ is the unit normal along the z-direction and $\mathscr{M}$ is the constant mass of the drop. A simple rearrangement of terms and simplification shows that equations (3.8) and (3.20) are exactly identical as $We_d \to 0$. Balancing the capillary pressure due to the curvature with the pressure drop across the interface we obtain the following equation,

$$2\mathscr{D} + \frac{\mathrm{d}}{\mathrm{d}\eta}\left[(1-\eta^2)\frac{\mathrm{d}\mathscr{D}}{\mathrm{d}\eta}\right] = We_d^{-1/2}(p_g - p_\infty) + \frac{\partial \phi}{\partial t} - \frac{\mathrm{d}W}{\mathrm{d}t}\eta + O(We_d^{1/2}\mathscr{D}).$$

Using the fact that $\mathscr{D}$ is expressible as a linear superposition of Legendre modes, the above equation can be rewritten as:

$$\sum_{k=2}^{\infty} \frac{\mathrm{d}B_k}{\mathrm{d}t}\mathscr{P}_k(\eta) = \frac{\mathrm{d}W}{\mathrm{d}t}\mathscr{P}_1(\eta) - We_d^{-1/2}(p_g - p_\infty) - \sum_{k=2}^{\infty}(k^2 + k - 2)\mathscr{L}_k\mathscr{P}_k(\eta). \tag{3.21}$$

Multiplying (3.21) by $\mathscr{P}_m(\eta)$ and integrating over η from -1 to $+1$ we obtain (for $k \geqslant 2$):

$$\frac{\mathrm{d}B_k}{\mathrm{d}t} = -(k^2 + k - 2)\mathscr{L}_k - \frac{2k+1}{2}We_d^{-1/2}\int_{-1}^{1}(p_g - p_\infty)\mathscr{P}_k(\eta)\,\mathrm{d}\eta. \tag{3.22}$$

Note that for this equation to be consistent with the expansions assumed for ϕ and $\mathscr{D}$ we need:

$$\frac{\mathrm{d}W}{\mathrm{d}t} = \tfrac{3}{2}We_d^{-1/2}\int_{-1}^{1}(p_g - p_\infty)\mathscr{P}_1(\eta)\,\mathrm{d}\eta.$$

It can be easily checked that this equation is satisfied in the limit $We_d \to 0$. In addition, we also require that the zeroth Legendre moment of the scaled excess gas

pressure be zero, i.e.

$$\int_{-1}^{1}(p_g - p_\infty)\mathscr{P}_0(\eta)\,\mathrm{d}\eta = \int_{-1}^{1}(p_g - p_\infty)\eta\,\mathrm{d}\eta = 0.$$

This equation is satisfied since the component of the excess pressure that is independent of the angular variable and constant is identically zero. Equations (3.19) and (3.22), when solved simultaneously with appropriate initial conditions, yield the deformation and velocity profiles. The viscous dissipation in the drop both in the inner and outer regions has been neglected.

3.2.3. *Matching and calculation of the unknown function $f(t)$*

In order to obtain a uniformly valid description of the drop deformation we functionally match the inner and outer solutions for the deformation and thus obtain $f(t)$. The matching region in terms of the angular variable θ (or in terms of r) satisfies $\max(Ca_g^{1/4}, We_d^{1/4}) \ll \sin\theta \ll 1$, that is, $\max(1, St^{1/4}) \ll r \ll Ca_g^{-1/4}$. For a separation of scales to exist, the asymptotic theory we developed is thus restricted to the range of Stokes numbers $St \ll Ca_g^{-1}$, i.e. $We_d \ll 1$ and is consistent with the assumptions made. Seen from the outer region, the inner and matching regions tend to the origin $r = 0$ in the limit of vanishing capillary and Weber numbers. Rewriting equation (3.22) and using the fact that points in the inner region correspond to very small values of θ, we obtain:

$$\frac{\mathrm{d}B_k}{\mathrm{d}t} = -(k^2 + k - 2)\mathscr{L}_k - \frac{2k+1}{4\pi}\frac{a}{\sigma}\frac{We^{-1/2}}{a^2}\left[2\pi\int_0^{r'_\infty}(p'_g - p'_\infty)\mathscr{P}_k\left(1 - \frac{1}{2}\frac{r'^2}{a^2}\right)\left(1 - \frac{1}{2}\frac{r'^2}{a^2}\right)^{-1} r'\,\mathrm{d}r'\right].$$

Taking the leading expansion of the integrand, we obtain (see Appendix A):

$$\frac{\mathrm{d}B_k}{\mathrm{d}t} = -(k^2 + k - 2)\mathscr{L}_k - \frac{2k+1}{3}\frac{\mathrm{d}W}{\mathrm{d}t}. \tag{3.23}$$

Equations (3.19) and (3.23) together with appropriate initial conditions are sufficient to determine the values of $\mathscr{L}_k$ for all time. Combining the two gives us a second-order equation for $\mathscr{L}_k$ which can be solved exactly. The solution is as follows:

$$\mathscr{L}_k(t) = \sin(\omega t)c_1(k) + \cos(\omega t)c_2(k) - \frac{2k^2+k}{3\omega}\int_0^t\left[\frac{\mathrm{d}W(t')}{\mathrm{d}t'}\cos(\omega t')\sin(\omega t)\right]\mathrm{d}t' - \frac{2k^2+k}{3\omega}\int_0^t\left[\frac{\mathrm{d}W(t')}{\mathrm{d}t}\sin(\omega t')\cos(\omega t)\,\mathrm{d}t'\right], \tag{3.24}$$

where, $\omega(k) = (k^3 + k^2 - 2k)^{1/2}$. The first two terms on the right hand-side represent undamped free surface oscillations corresponding to capillary waves on the surface of the drop. The constants in these two terms, $c_1(k)$ and $c_2(k)$ are to be determined from the initial conditions when the force acting on the drop is zero (namely, at large separations). We note that the deformation has been scaled by $aWe_d^{1/2}$. At large separations, the deformation of the drop is typically $O(aCa_g)$ and hence $\mathscr{L}_k(t=0) \sim O[(Ca_g/St)^{1/2}] \ll 1$. Thus, suitable initial conditions valid when $Ca_g^{1/2} \ll 1$ and $St > 1$ are $\mathscr{L}_k = 0$ and $\mathrm{d}\mathscr{L}_k/\mathrm{d}t = 0$ at $t = 0$. The third and fourth terms on the right-hand

side of (3.24) represent the direct effect of the force and also the wavelike deformation created owing to the forcing. These expressions have a component that is in phase with the forcing and an oscillatory component that is out of phase. Analysis of (3.24), or equivalently analysis of equations (3.19) and (3.23) in the limit of large n, indicates that the deformation modes for large n go as:

$$\mathscr{L}_k(k \gg 1) \approx -\frac{2}{3}\frac{\mathrm{d}W}{\mathrm{d}t}\frac{1}{k} + O\left(\frac{\mathrm{d}W}{\mathrm{d}t}k^{-2}\right). \tag{3.25}$$

Thus, the large deformation modes behave as in the idealized problem dealt with in § 2 and are in quasi-static equilibrium with the forcing.

Rewriting the expression for the deformation given by the lubrication asymptote and equating it to the deformation given by the Legendre expansion, we obtain:

$$-D(\theta) = \frac{1}{3}\frac{\mathrm{d}W}{\mathrm{d}t}\ln(Ca_g^{-1/2}) + \frac{2}{3}\frac{\mathrm{d}W}{\mathrm{d}t}\ln(\sin\theta) - f(t) = \mathscr{D}(\theta) = \sum_{k=2}^{\infty}\mathscr{L}_k\mathscr{P}_k(\cos\theta). \tag{3.26}$$

We now write the sum over all modes as follows using the fact that for large k, we may replace the summation by an integral:

$$\sum_{k=2}^{\infty}\mathscr{L}_k\mathscr{P}_k(\eta) = \sum_{k=2}^{N_c}\mathscr{L}_k\mathscr{P}_k(\eta) + \int_{N_c}^{c(\sin\theta)^{-1}}\mathscr{L}_k\mathscr{P}_k(\eta)\,\mathrm{d}k + \int_{c(\sin\theta)^{-1}}^{\infty}\mathscr{L}_k\mathscr{P}_k(\eta)\,\mathrm{d}k, \tag{3.27}$$

where c is an $O(1)$ constant, $\eta = \cos\theta$ and N_c is a cutoff number that satisfies:

$$1 \ll N_c \ll c(\sin\theta)^{-1}.$$

To evaluate the integrals and obtain a closed form expression for $f(t)$ we must substitute analytical forms for the Legendre polynomials in (3.27). The following expressions for the Legendre polynomials are very accurate (see Tsao & Koch 1994)

$$\mathscr{P}_k(\cos\theta) \approx 1 - \tfrac{1}{2}(k^2+k)(1-\cos\theta) + \tfrac{1}{16}(k^2-1)(k^2+2k)(1-\cos\theta)^2, \quad (k\sin\theta)^4 \leqslant 64$$

$$\mathscr{P}_k(\cos\theta) \approx \frac{\cos(k\theta+\frac{1}{2}\theta) + \sin(k\theta+\frac{1}{2}\theta)}{\sqrt{\pi k\sin\theta}}, \quad (k\sin\theta)^4 > 64$$

and we use these expressions. This corresponds to choosing the value $c = 8^{1/2}$. In order to complete the matching procedure we must show that the sum of the deformation modes has a term that diverges as $\ln(\sin\theta)$. Substituting these asymptotic expressions for $\mathscr{P}_k$ in (3.27) and simplifying the resulting integrals in the limit $\theta \to 0$, we find that, indeed, in the limit $\theta \to 0$ the logarithmically divergent terms match and $f(t)$ is completely specified once the next $O(1)$ term is evaluated. After some algebraic manipulations we finally obtain

$$f(t) = \frac{\mathrm{d}W}{\mathrm{d}t}\left[\tfrac{2}{3}\ln\left(\frac{Ca_g^{-1/4}}{N_c}\right) + 0.100\ldots\right] - \sum_{k=2}^{N_c}\mathscr{L}_k. \tag{3.28}$$

The final expression for $f(t)$ is actually independent of N_c provided that N_c lies in the range of values mentioned above.

A brief note on the errors involved and the range of applicability of this analytical matching result is in order. The leading term in the sum of the deformation modes is $O(\ln(\sin\theta))$. Since the matching region is beyond the dimple region, this leading

term is typically $O(\ln(We_d^{-1/4}))$. The higher-order corrections are thus typically $O(1)$, $O(We_d^{1/4})$ and so on. When $\ln(We_d^{-1/4}) \gg 1$, the neglect of higher-order terms leads to negligible error and the analytical expression for $f(t)$ is quite accurate. However, when the Weber number is not so small, the higher-order terms cannot be neglected and a numerical matching has to be performed. The use of the simple analytical form (3.28) can, in such cases, lead to inaccurate and unphysical solutions.

3.3. *Collisions of a droplet with a rigid planar wall*

A situation encountered in many physical applications is collision of droplets with rigid planar walls. One example is high-pressure sprays where the drops are surrounded by a pressurized gas. We can use an analysis similar to that presented thus far to study the rebound dynamics of the colliding drops in the limit of low impact energy. In fact, the drop–drop collision may be regarded as a drop–wall collision (the wall being rigid) with a zero stress condition, instead of perfect stick conditions at the wall. Mathematically, instead of imposing the condition that the velocity be zero at the wall, we would need to impose the condition that the derivative of the velocity is zero at the wall. Note that we could equivalently use the method of images to formulate the governing equations appropriate for the Stokes flow in this case.

Let the rigid wall be coincident with the $z = 0$ plane (figure 1*a*) and consider drop 2 with undeformed radius a as the drop undergoing a normal head-on collision with the wall. We make the scalings as in the drop–drop case. The expression for the gap in the near-contact region is now given by:

$$H_{dw} = h + \tfrac{1}{2}r^2 + \left(\frac{We_d}{Ca_g}\right)^{1/2} D. \tag{3.29}$$

The equations for the flux j, the centre of mass velocity W and the equation for the deformation D are the same as before. The boundary conditions and the large r behaviour of D are identical to those obtained for the droplet collision problem. The only difference is in the equation for the evolution of the gap size H_{dw} which has the form:

$$W + \frac{\partial D}{\partial t} = \frac{1}{12}\frac{1}{r}\frac{\partial}{\partial r}\left(rH_{dw}^3 \frac{\partial p_g}{\partial r}\right). \tag{3.30}$$

Comparison to the drop–drop case shows that the numerical factor multiplying the right-hand side of (3.30) is different from that in (3.5). This reflects the fact that only the drop–gas interface can deform and thus has a non-zero normal velocity component. In fact, a suitable rescaling of the variables and the initial conditions renders the two equations for the gap evolution identical. The above equations imply that for large values of r, the pressure profile is given by the following asymptotic relationship

$$p_g(r \gg 1) \sim -\frac{12}{r^4}\left(W + \frac{\partial D}{\partial t}\right).$$

4. Results and discussion

The equations for the gap thickness and the deformation given by (3.5) and (3.10) form a coupled nonlinear elliptic–parabolic system of equations. The boundary condition on H, i.e. (3.12), introduces further complications in the attempt to find a suitable convergent and accurate numerical scheme. This is because the deformation

in the outer region depends on the force acting on the drop and hence the matching constant $f(t)$ is also an unknown quantity. Explicit methods to solve the equations in the incompressible limit and for finite β are not very useful since the stability limit on the maximum allowable time step Δt is seen to scale as $(\Delta r)^4$. Thus, for $\Delta r \sim O(10^{-2})$ the minimum time increment will be $O(10^{-8})$ and prohibitively small. An adaptation of the predictor–corrector scheme outlined in our paper for rigid particles (Gopinath, Chen & Koch 1997) showed that this requirement for the largest possible time step for obtaining stable solutions was indeed true. This is, in fact, not surprising since the equations we are trying to solve constitute a set of stiff thin-film equations. The simple predictor–corrector method based on the trapezoidal rule was seen to be second-order accurate in time, but it had roughly the stability of the explicit Euler method, i.e. $(\Delta t)_{min} < (\Delta r)^4$. Since explicit schemes did not give good results, implicit schemes were then tried. The completely implicit, iterative scheme used by Davis, Serayssol & Hinch (1986) and also by Yiantsios & Davis (1990) was tried. To guarantee convergence for very strong deformations, under-relaxation had to be used because of the inverse non-evolutional order of operations employed. This method was seen to work well for $O(1)$ values of the Stokes number. However, for large Stokes numbers, a very small value of the under-relaxation parameter was required and a prohibitively large number of iterations was required to obtain accurate results. Consequently, we used a semi-implicit direct, matrix method based on the algorithm described in Rother, Zinchenko & Davis (1997). This allowed us to obtain stable, accurate solutions using a reasonable number of grid points without resorting to extremely small time steps. The iterative scheme was used to validate and check the accuracy of the matrix inversion results. Details of the numerical algorithm and the code are given in Appendix B.

We present numerical results for Capillary numbers, $Ca_g = 10^{-8}$–10^{-5}. These values are small enough that meaningful comparisons can be made with the idealized problem solved in § 2. At the same time, they represent physically meaningful values representative of real collisions. The Stokes numbers we study range from 2 to 200. Equations (3.3)–(3.11) indicate that the natural dimensionless quantity that enters as an independent scaling parameter is not the Stokes number, but rather $(We_d/Ca_g)^{1/2} = \chi$. We present most of our results in terms of Ca_g and χ. The Stokes number is simply $2\chi^2/9$. All values of Ca_g that we consider are small enough for the lubrication calculations to be started assuming nearly undeformed spheres. In order to obtain estimates of the deformation prior to the development of lubrication flow, the deformation and pressure profiles for some values of St and $Ca_g = 10^{-6}$ were calculated using the outer trajectory analysis of § 3.1. These calculations were started at an initial centre to centre distance of $3a$ and continued until $h = 20$, after which the lubrication equations were used. We found that in all cases, so long as $Ca_g^{-1/2} \gg 1$, ignoring this initial deformation and instead using the deformed profile obtained from a regular perturbation analysis of the lubrication equations did not change our results significantly. All our calculations were started using the initial condition $h(t = 0) = 15$ and $W(t = 0) = -1$. The initial deformation of the spheres is small in all the cases we considered and hence we used the undeformed parabolic profiles as the initial interface shapes in our trajectory calculations. Consequently, the initial condition for the fluid and deformation modes in the outer region were $\mathscr{L}_k = 0$ and $\mathrm{d}\mathscr{L}_k/\mathrm{d}t = 0$ for $k \geqslant 2$ at $t = 0$. We will compare our analysis and results with existing theoretical results for two classes of problems that have similarities to inertia driven drop collisions. One is buoyancy-driven coalescence of slightly deformable drops in a viscous liquid, which has been investigated in various papers over the last few years. In this case, there are no inertial effects and the force driving the drops

together is determined by the orientation of the drops relative to the gravity† vector. Effects of particle inertia have also been investigated in so-called elastohydrodynamic (Davis *et al.* 1986; Serayssol & Davis 1986; Barnocky & Davis 1989) collisions of solid deformable particles in an ambient liquid. Studies demonstrating the influence of pressure-dependent liquid density and viscosity on the dynamics of low-Reynolds-number collisions of elastic and rigid spheres indicate that there is significant coupling between the equations describing the fluid dynamics in the gap and the elastic solid mechanics in the particles. These studies show that a dimple is formed on the sphere surface during the collision process and the spheres rebound without coming into contact. In fact, for Stokes numbers larger than a critical value, the spheres were seen to bounce back to their initial separations.

We perform calculations of two types. In one type, the Capillary number Ca_g is held fixed and the Stokes number is varied. This is equivalent to varying the Weber number at fixed Capillary number. Since the dynamical trajectory calculations are mapped in terms of scaled time, it should be remembered that to obtain the dimensional time we must multiply by $a\,We_d^{1/2}\,U_c'^{-1}$. A decrease in the scaled time owing to an increase in χ does not necessarily mean a decrease in dimensional time. We also perform some calculations keeping χ fixed, but varying the Capillary number. In this case too, the Weber number changes and conversion to dimensional times should be made accordingly.

4.1. *Small deformation results*

For a fixed and small value of the Capillary number, a larger fraction of the initial energy is stored as deformation energy as the Stokes number increases. This trend is almost independent of Ca_g as long as $Ca_g \ll 1$. Thus, for small Stokes numbers, we anticipate that the extent of deformation is small and the drops behave as nearly rigid spheres. This rigid sphere behaviour is seen for drops which do not have sufficient energy to come to within an $O(a\,Ca_g)$ distance of each other. Figure 7 is a plot of the minimum distance between the spheres H_{min} (the solid line) as a function of scaled time t. For all the results shown, the Capillary number Ca_g is 10^{-6}. Profiles are shown for $\chi = 0.25$–1.5. If the drops were truly rigid, incompressible lubrication theory predicts that the minimum distance would be:

$$H_{min}^{inc} = H_{min}^{inc}(t=0)\exp(-\tfrac{8}{9}\chi^2) = 2h(t=0)\exp(-\tfrac{8}{9}\chi^2), \tag{4.1}$$

and these values are shown as filled circles on the same graph. We find that for $\chi = 0.25$ and 0.5, the drops indeed behave as nearly rigid spheres. For $\chi = 1.0$ and 1.5, we find that the drops actually come to a halt at a separation that is lower than that predicted by equation (4.1).

At small St and at fixed and small but non-zero value of Ca_g, the drop surface deforms slightly and this allows a larger gap and less energy dissipation during the approach. The effect should vanish as Ca_g goes to zero. We find that for $\chi > 2$, the minimum distance of approach is greater than that predicted for rigid spheres

† In studies by Rother *et al.* (1997) and Yiantsios & Davis (1990), the evolution of the buoyancy-driven drop is traced from a relatively undeformed state until a dimple forms and a long-time quasi-steady pattern is established. The constant buoyancy force and negligible drop inertia imply that the long time drop deformation and dimple behaviour are independent of initial conditions. Owing to the quasi-steady nature of the flow and deformation profiles that develop, we can employ a singular perturbation analysis, using fractional powers of inverse time as the small parameter, to obtain scaling relationships for the drop temporal evolution of the gap thickness and dimple extent. This approach is, however, ruled out when effects of drop inertia cannot be neglected.

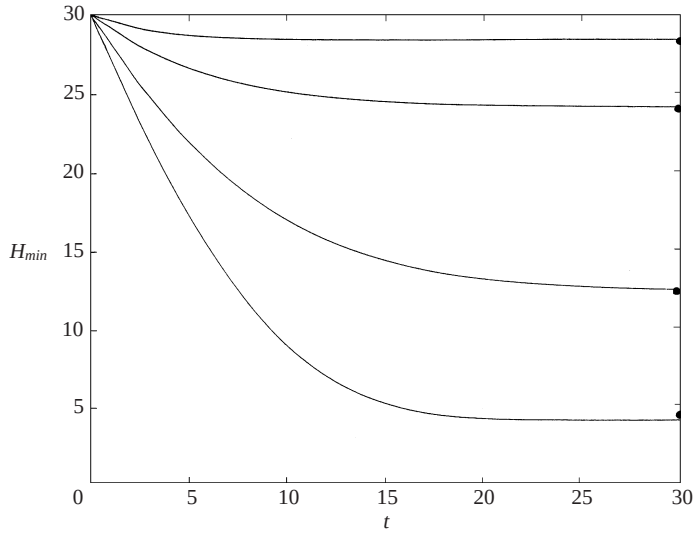

FIGURE 7. Small deformation results: temporal evolution of the minimum gap thickness, $H_{min}(t)$, for $Ca_g = 10^{-6}$ and χ (from top to bottom) of 0.25, 0.5, 1.0 and 1.5. ●, Predictions of rigid sphere theory given by equation (4.1).

owing to stronger surface deformation. Figure 8 shows the variation of the minimum gap thickness as a function of the centre of mass velocity, W. The solid curves are our numerical results. The Capillary number $Ca_g = 10^{-6}$ and χ (for curves from top to bottom) is 0.5, 1.0, 1.5 and 2.0. The dashed curves are predictions of lubrication theory for a rigid sphere collision:

$$W = -1 + \frac{9}{8\chi^2} \ln\left(\frac{h(t=0)}{h(t)}\right). \tag{4.2}$$

Note that for a rigid sphere, $H_{min}(t) = 2h(t)$. Also, equation (4.2) indicates that the minimum gap thickness is reached when the velocity (and consequently the force) goes to zero. We see that, as before, for $\chi = 0.5$ and 1.0, the drops behave as nearly rigid spheres and for these values of χ, the velocity goes to zero as the force becomes zero. For $\chi = 1.5$, slight effects of surface deformation are seen and the results begin to deviate from the rigid sphere result. In all these three cases, the spheres come to a rest at separations greater than one. For $\chi = 2$, the results deviate significantly from the rigid sphere results. The minimum distance between the spheres is reached not when the spheres come to a halt, but rather during the approach process at $t \approx 15$. A reasonably large fraction of the initial energy is stored as surface deformation energy. This energy when released causes the drops to bounce back significantly and finally come to rest at an equilibrium dimensionless separation of approximately 0.85 which is slightly less than that predicted by equation (4.1). The oscillatory behaviour of the centre of mass velocity and position is also well illustrated in the same figure.

4.2. *Collision and rebound dynamics for moderate and large Stokes numbers*

For small deformations ($h \gg 1$) we can use a regular perturbation analysis to obtain the following expressions valid during the initial stages of approach:

$$p_g(r,t) \approx -\frac{3W}{(2h + r^2)^2}, \tag{4.3}$$

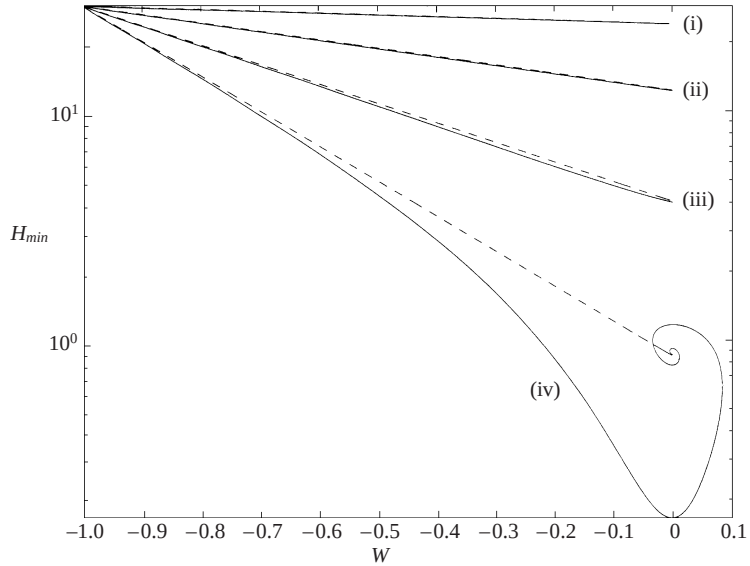

FIGURE 8. Small deformation results: variation of the minimum gap thickness as a function of the centre of mass velocity, W. The capillary number $Ca_g = 10^{-6}$ and χ (from top to bottom) is 0.5, 1.0, 1.5 and 2.0. The solid curves are our numerical results and the dashed line corresponds to equation (4.2).

$$\frac{\mathrm{d}W}{\mathrm{d}t} \approx -\frac{9W}{8\chi h}, \tag{4.4}$$

$$D(r,t) \approx \frac{3W}{8\chi h}\ln(2h + r^2) + f(t). \tag{4.5}$$

Equation (4.2) indicates that collisions between drops with χ much greater than approximately $(9\ln(h(t=0))/8)^{1/2}$ will lead to a rebound. This is consistent with our calculations which indicate that for $\chi > 2$, the drops deform strongly and a significant portion of the initial kinetic energy is stored as deformation energy.

In order to illustrate clearly the interesting aspects of the collision process, we examine in detail two cases corresponding to $\chi = 3$ ($St = 2$) and $\chi = 20$ ($St \approx 88.8$). For both of these, $Ca_g = 10^{-6}$ and the initial conditions were, as before, $h(t=0) = 15$ and $W(t=0) = -1$. Thus, χ is changed by changing We_d. The initial deformation was set to zero and the temporal evolution of the pressure, deformation, gap thickness, centre of mass velocity and scaled force was analysed. An examination of these variables in conjunction provides a composite and complete picture of the approach and rebound process.

Consider first the collision dynamics for $\chi = 3$ illustrated in figure 9. The drops start with a minimum separation of $30(a\,Ca_g^{1/2})$ and a relative velocity of $2U_c'$ directed towards each other. As the drops approach, the gas in the intervening film resists the relative motion of the drops and generates a force that decelerates the centroids. The deformation during the initial stages of approach when $h \gg 1$ is negligible and hence the evolution of the gap, the force on the drops and the pressure profiles generated follow trends predicted by equations (4.3)–(4.5). The deformation and the flow generated in the interior of the drops are small for $0 < t < 6$, t being the scaled time. The decrease in the kinetic energy of the centroids is mostly due to viscous dissipation in the gas film. Both the minimum gap thickness and the

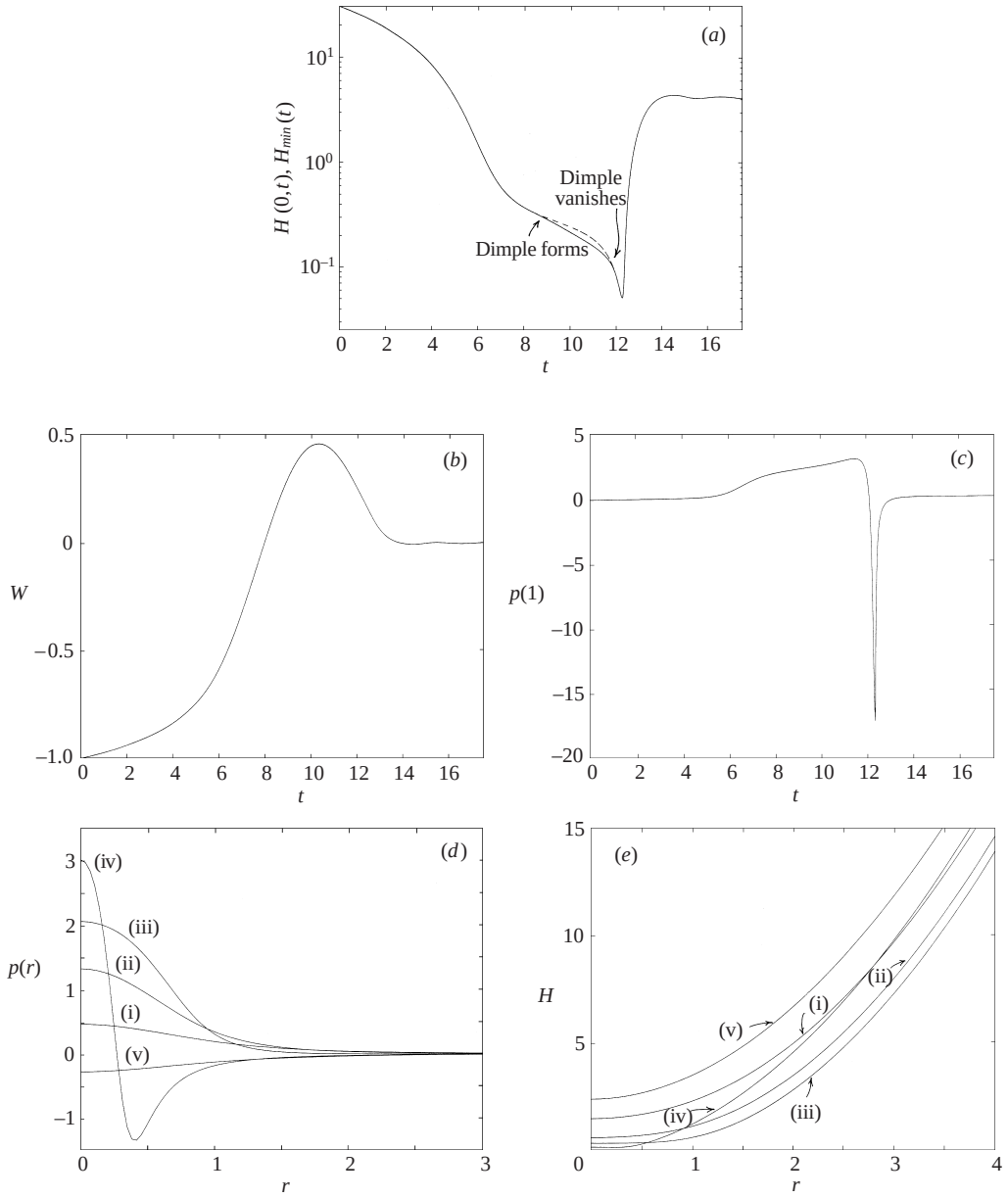

FIGURE 9. Plots of (a) minimum gap thickness, H_{min} (solid line) and the centreline separation, $H(r = 0, t)$ (dashed line), (b) centre of mass velocity, $W(t)$, and (c) the centreline pressure $p_g(1) = p_g(r = 0, t)$ for the duration of the collision. Also shown are (d) pressure profiles, $p_g(r, t)$, and (e) gap profiles, $H(r, t)$, at various instants. The curves correspond to profiles at dimensionless times (i) $t = 6$, (ii) 7, (iii) 8.5, (iv) 11.5 and (v) 13. The capillary number is $Ca_g = 10^{-6}$ and $\chi = 3$.

maximum pressure occur at the centreline. The gap thickness and pressure profiles are monotonic functions of r. At time $t \approx 6$, the near-contact region around $r = 0$ begins to flatten considerably. The minimum gap thickness is approximately 1.3. Instead of causing an increased radial flux away from the centreline, the relative motion of the drops causes rapid deformation of the drop interfaces. This behaviour

is similar to the near contact motion of rigid spheres in a compressible gas where the gas tends to compress rather than flow out of the gap. The tendency of the drops to deform manifests itself in the decreased rate at which the minimum gap thickness H_{min} decreases. The rate of change of the force begins to decrease and both the velocity and the force profiles exhibit points of inflection. The pressure profiles begin to show a characteristic inner region where the gas pressure is $O(1)$ and an outer region where the pressure is much less than 1. In the outer region, the pressure and deformation are given by the asymptotic forms (3.12) and (3.13). The decreasing gap separation causes the pressure and deformation to become more localized, as is evident from the steepening of the profiles in figures 9(d) and 9(e) at $t = 7$. A dimple begins to form at a dimensionless time of $t \approx 8.2$ and the minimum gap separation occurs at the rim of the dimple rather than at $r = 0$. At this point, the centreline pressure is approximately 2 indicating that the pressure in the dimple area close to $r = 0$ is $p'_\infty + 2\sigma/a$ to leading order. The formation of the dimple causes a larger curvature at the rim compared to the centreline and consequently, the gas film thins faster at the rim owing to the relatively larger pressure gradient. Thus, H_{min} decreases faster than $H(r = 0, t)$. Most of the total force acting on the drops comes from the $O(1)$ pressure in the dimple region. Note, however, that the centre of mass velocities have, by this time, reversed sign so that the centroids are actually moving away from each other even though the near-contact regions are moving towards one another. An examination of the global drop deformation indicates that the drops become flattened at the end (around $\theta = \pi$) and bulge out at the equator (around $\theta = \frac{1}{2}\pi$) at this time. The dimple meanwhile increases in extent and reaches a maximum radial width of approximately 0.46 at $t \approx 9.9$. Note that although the film thickness remains approximately $O(aCa_g^{1/2})$, the centroid to centroid distance becomes less than $2a$ by an amount $O(aWe_d^{1/2})$. As the dimple width begins to decrease, a larger fraction of the initial kinetic energy that is stored has been channelled back into the energy corresponding to the translational mode, i.e. the centre of mass speed increases. The motion of the drops away from each other causes the interfaces beyond the dimple region to peel away from the plane of symmetry corresponding to $z = 0$. This motion occurs rather rapidly and leads to an adverse pressure gradient and a pressure that is less than the ambient pressure over the region beyond the dimple rim. Thus, at time $t = 11.5$, the pressure profile is non-monotonic. It has two extrema, a maximum positive value at $r = 0$ and a minimum negative value just beyond the dimple. As the dimple shrinks, the force acting on the drops decreases and the radial region over which $p_g > p_\infty$ decreases. The centreline pressure is still of the order of 2. The radial flux out of the centreline region causes the separation at $r = 0$ to decrease with time and a tail to form. This tail then pushes into the gap, resulting in a minimum film thickness with respect to time (primary minimum, H^*_{min}) that occurs at $t \approx 12.2$. Meanwhile, when $t \approx 12$, the dimple vanishes and the minimum film thickness once again occurs at $r = 0$. The excess gas pressure at all points in the gap now rapidly becomes less than p'_∞. This causes a flux of gas into the gap which together with the relaxation of the surface deformation causes the tail to retract back in a very short period of time. In fact, the tail formation and retraction occurs in a short time interval that is $\Delta t \approx 0.8$, compared to the time $\Delta t \approx 6$ for which the dimple exists. By this time, the centre of mass velocity starts to decrease quite rapidly owing to the large negative force acting on each of the drops. As the drops move away from each other, the interplay and exchange of energy between the deformation and the translational modes causes the centroids to execute an oscillatory behaviour. In this case, we see that the residual energy remaining after the drops have rebounded back to beyond $H_{min} = 2$ is rapidly dissipated. Eventually,

the drops come to a rest at a dimensionless separation of approximately 3.5. Thus, this entire collision process may be considered one with an effective coefficient of restitution of zero since all the initial kinetic energy is dissipated and the drops do not rebound back to their initial separations. The net force acting on the drops slowly increases from zero at $t = 0$ and reaches a positive maximum at $t \sim 7.8$, after which it decreases. The force then becomes negative at $t \sim 10.2$ decreases further due to the negative pressure gradient in the thin gap, attains a negative minimum at $t \sim 12.3$ and then slowly increases to zero with pronounced oscillations as the drops come to a stop.

In order to investigate the dynamics at large Stokes numbers, we conducted trajectory calculations for the case where $\chi = 20$ and the capillary number was 10^{-6}. The initial conditions were the same as for the $\chi = 3$ case, i.e. $h(t = 0) = 15$ and $W(t = 0) = -1$, and the initial profiles were those for rigid spheres. Figure 10 shows the temporal evolution of various quantities during the entire collision process. In this case, we terminated our calculations when the drops rebounded back to their initial separation. For small times, the dynamical behaviour was predicted well by the small deformation equations, namely (4.3)–(4.5). We expect that the initial approach before deformation is important, is faster than for the $\chi = 3$ case and that the drops approach to within an $O(aCa_g^{1/2})$ distance of each other in an $O(aCa_g^{1/2}U_c^{-1})$ time owing to negligible viscous dissipation in the gas film. In terms of scaled time, the initial approach occurs in a time of $O(\chi^{-1})$ for $\chi \gg 1$. The force acting on the drops during the initial stages is quite small and causes negligible deformation. The increasing centreline pressure eventually causes flattening of the surface around $r = 0$. A rather rapid increase in the centreline pressure occurs around $t \approx 0.8$. The value of h becomes zero at this point indicating that if the drops were rigid they would have overlapped at this point. The centreline pressure begins to increase rapidly. At $t \approx 0.99$, a dimple forms. The pressure at the centreline is slightly more than 2 at this point but the profile is still evolving. Once the dimple forms, the centreline separation remains almost constant and changes very slowly. The separation at the rim, on the other hand, decreases at a significantly faster rate owing to the large local pressure gradient in the gas and a smaller radius of curvature. The pressure and deformation profiles indicate that the force on the drop increases mainly due to the lateral spreading of the dimple. The centreline pressure remains almost constant, but the motion of the drop squashes the near-contact surface thus leading to an increase in dimple radius. The radial pressure profiles tend to a step shape with a near constant value in the dimple and with a sharp gradient at the rim. Beyond the dimple, the pressure drops extremely rapidly to the asymptotic value given by (3.13). Meanwhile, h reaches a minimum value of about -27.2 at $t \approx 2.92$. The centroids of the drops then begin to move away from each other. The minimum separation, however, continues to decrease and the dimple continues to spread attaining its maximum radial extent of about 3.03 at approximately $t = 3.3$. After this, the dimple width begins to decrease causing the force to decrease proportionately. The film thickness at the rim reaches a minimum with respect to time at approximately $t = 3.7$ and then begins to increase. The gap profile at this point ($t \approx 3.7$) clearly shows the large radius of curvature in the interior of the dimple. This minimum, which we did not observe in the $\chi = 3$ case, we term the secondary minimum and denote by H_{min}^{**}. The drops now begin to move apart slightly as the dimple relaxes by shrinking, the interfaces beyond the rim gradually peeling away from each other. An interesting phenomenon then occurs. The film thickness at the centreline begins to decrease while the film thickness at the rim begins to increase. This causes the centreline pressure

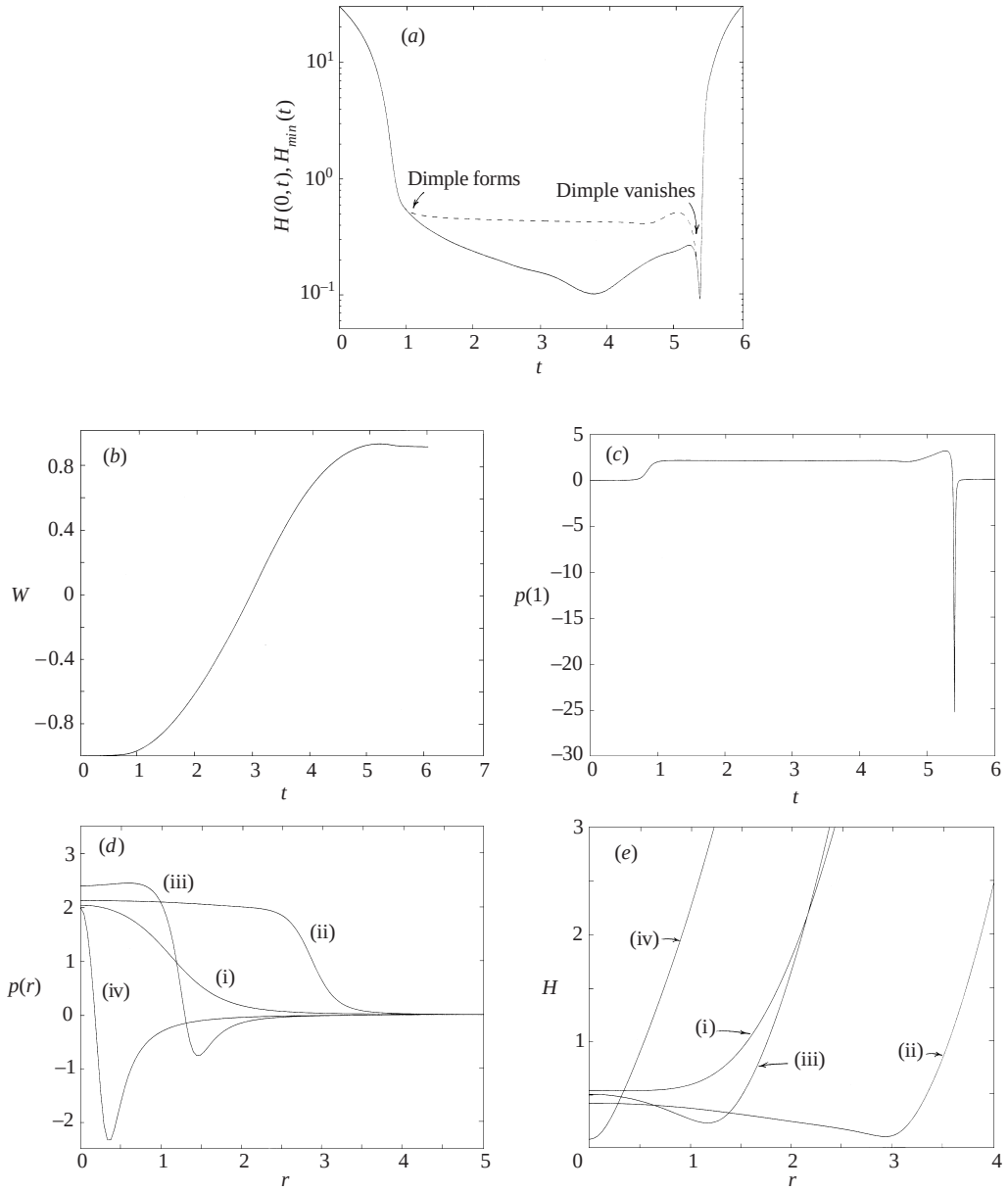

FIGURE 10. Plots of (a) minimum gap thickness, H_{min}, (solid line) and the centreline separation, $H(r = 0, t)$, (dashed line) (b) centre of mass velocity, $W(t)$, and (c) the centreline pressure $p_g(1) = p_g(r = 0, t)$ for the duration of the collision. Also shown are (d) pressure profiles, $p_g(r, t)$, and (e) gap profiles, $H(r, t)$, at various instants. The curves correspond to profiles at dimensionless times (i) $t = 1$, (ii) $t = 3.7$ and (iii) $t = 5$. Curve (iv) in the pressure plot corresponds to $t = 5.3$ and in the gap thickness plot corresponds to $t = 5.375$. The capillary number is $Ca_g = 10^{-6}$ and $\chi = 20$.

to increase while the pressure beyond the rim begins to attain values less than the ambient pressure (see profiles at $t \approx 5$). The front separating regions of positive excess gas pressure from the negative region rapidly moves towards the centreline leading to a force that becomes negative – from this point on, viscous effects begin to dominate. The dimple completely relaxes by $t \approx 5.37$; approximately the same time at which

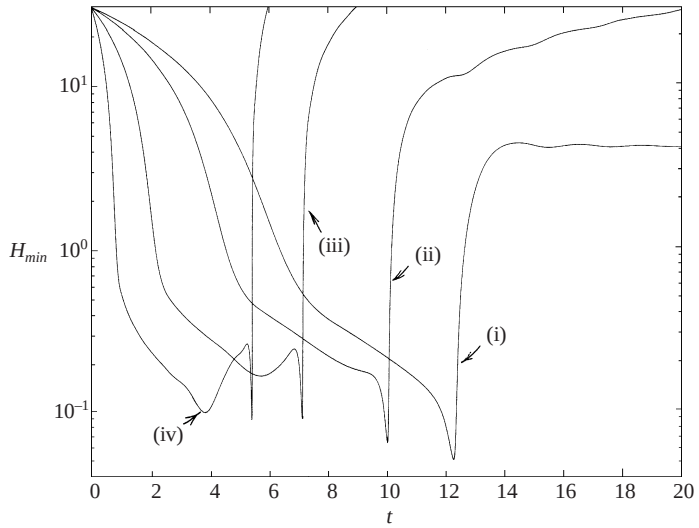

FIGURE 11. The temporal evolution of the minimum film thickness, $H_{min}(t)$, for various values of the scaled Stokes number χ and for a Capillary number of 10^{-6}. The curves from right to left correspond to (i) $\chi = 3$, (ii) 4, (iii) 8 and (iv) 20, respectively. As χ increases, the dimple formation becomes more pronounced and the secondary minimum that occurs during the dimple evolution process becomes smaller than the primary minimum that occurs when the tail begins to retract.

the centreline excess pressure becomes negative. Curve (iv) in the pressure profile plot illustrates clearly the small region of positive pressure followed by the region of negative pressure. The tail formation at $r = 0$ occurs because of the flux of gas out of the centreline region. The tail retraction occurs once the pressure in all of the lubrication region is less than ambient.

Figures 9 and 10 provide details of the collision process for two values of the Stokes number. The dynamical behaviour is seen to be strikingly different and it is of interest to enquire into the transition from the $O(1)$ to the $St \gg 1$ behaviour. Of particular relevance is the evolution of the minimum film thickness – the variation in the primary and secondary minima as the Stokes number (or equivalently χ) changes and their relative magnitudes. Figure 11 is a plot of $H_{min}(t)$ for trajectory calculations with $Ca_g = 10^{-6}$. The profiles (from right to left) correspond to increasing Stokes numbers. We see that for $\chi = 3$, there is no evidence of a secondary minimum. As the Stokes number increases, the dimple formation becomes more evident as indicated by the formation of an inflection point at $t \approx 9$ for $\chi = 4$. For larger Stokes numbers (curves (iii) and (iv)), the dimple evolution process is very easily identified. The plots indicate that the primary minimum (the sole minimum for small Stokes numbers) actually increases as the Stokes number increases. The secondary minimum, on the other hand, decreases as the Stokes number increases. Also, we see that the ratio of the time scale over which the tail retraction occurs to the time scale over which the dimple evolves becomes increasingly large as the Stokes number increases. Although not shown in the figure, our numerical results also indicate that for sufficiently large values of χ, the secondary minimum corresponds to a smaller gap thickness than the primary minimum.

Figure 12 shows the manner in which the dimple extent changes during the course of the collision for four values of χ. The Capillary number is set constant at 10^{-6}.

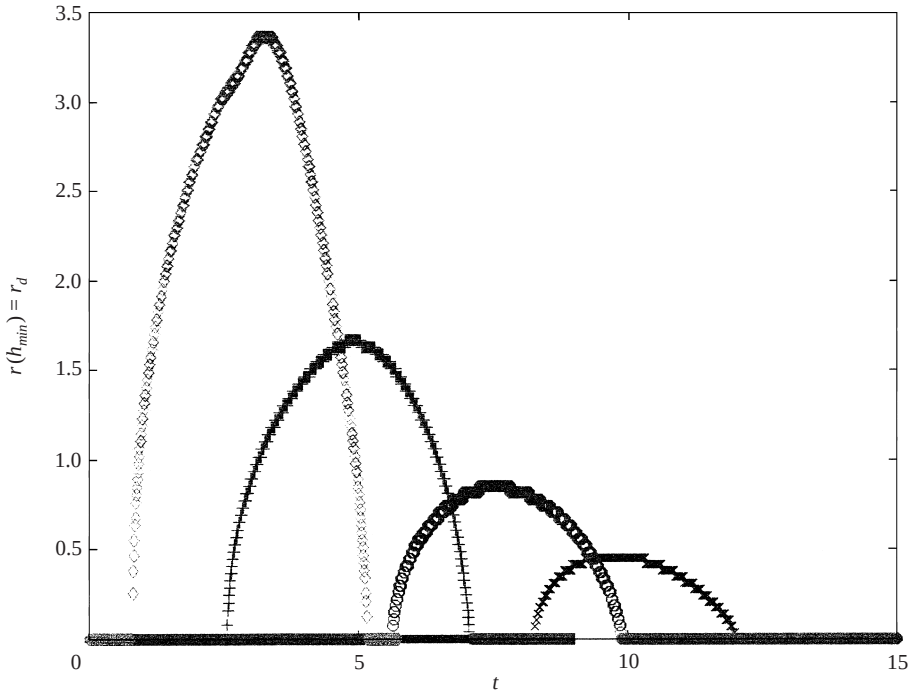

FIGURE 12. The temporal evolution of the dimple extent for values of χ (from right to left) of 3, 4, 8 and 24. The capillary number, Ca_g corresponding to these results isS 10^{-6}. The dimple widths have been scaled with $aCa_g^{1/4}$ and hence the maximum in these profiles increases as χ increases. The spacing between the symbols gives an idea of the temporal resolution of the results.

The onset of dimple formation takes place at a later scaled time for smaller values of χ. We expect that the smaller inertia leads to larger dissipation of the initial kinetic energy prior to deformation. This, in turn, results in a correspondingly smaller rate of increase in the centreline pressure. The dimple widths have been scaled with $aCa_g^{1/4}$ and hence the maximum in these profiles increases as $O(\chi^{1/2})$ with increasing χ. The scaled time for which the dimple exists seems to be almost constant for the different Stokes numbers shown in the figure. This will be discussed in greater detail in the following subsection. The profiles clearly illustrate how the fraction of the initial energy dissipated due to viscous effects increases as the Stokes number decreases. Also, we see that the asymmetry between dimple formation and dimple relaxation becomes more pronounced as χ increases. This is in accordance with the results of § 2 where we found that as the Weber number increased from zero, the collision and rebound took different times. Evidently, this effect persists for non-zero values of the capillary number.

4.3. *Effects of varying capillary number on the rebound phenomena*

Until now we have studied the Stokes number dependence of the collision process for a fixed value of the capillary number. The governing equations (3.5), (3.7), (3.10), (3.19) and (3.22) do not contain the capillary number explicitly as a parameter. However, the expression for $f(t)$ has a term that depends on $\ln(Ca_g)$ and thus it is of interest to study the variation in the results as the capillary number increases from zero. We first consider the minimum gap thickness at which the dimple forms, shown in figure 13(a)

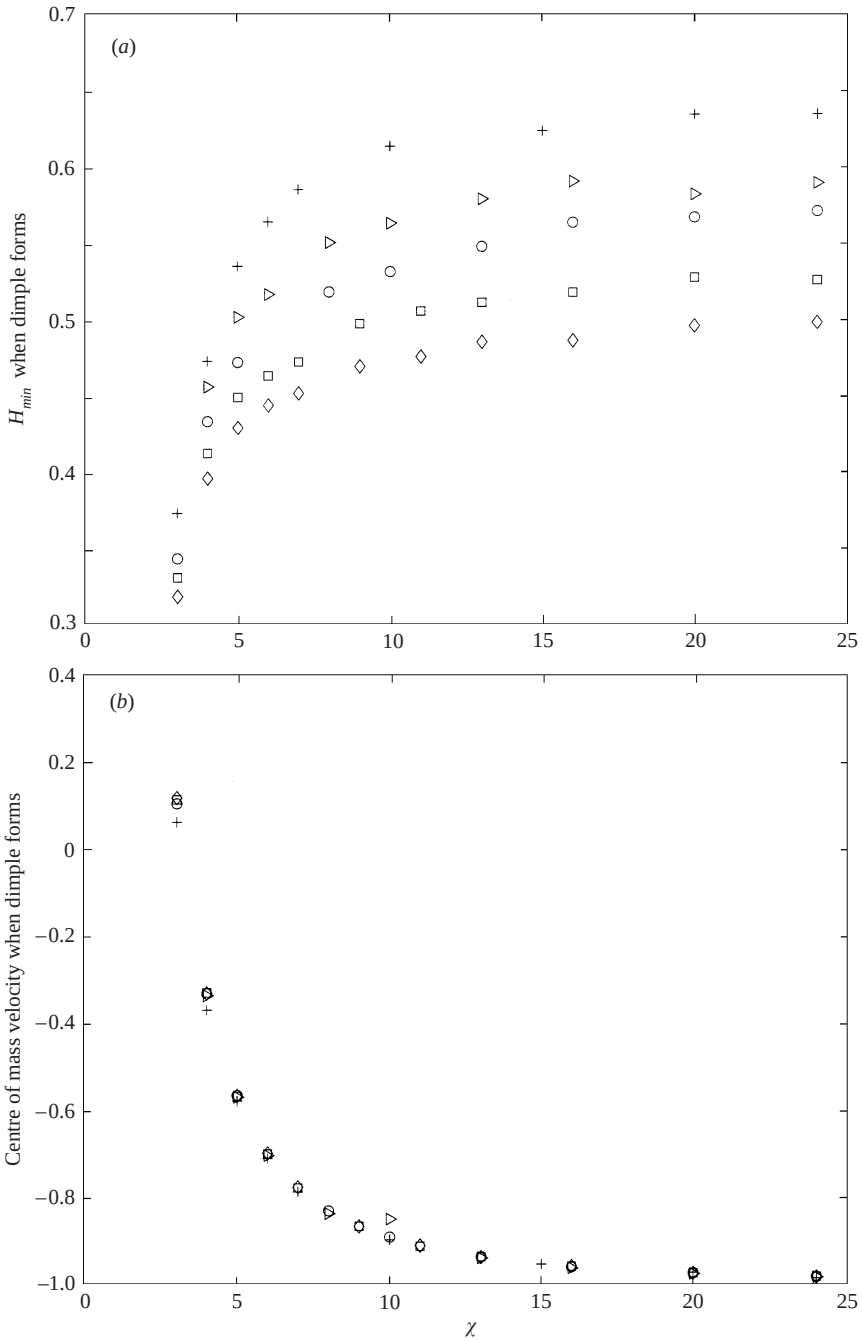

FIGURE 13. Values of (a) the minimum film thickness, H_{min}, and (b) the centre of mass velocity, W, when the dimple forms. ◇, $Ca_g = 10^{-8}$; □, 10^{-7}; ○, 10^{-6}; △, 10^{-5}; ×, $Ca_g = 10^{-4}$.

for capillary numbers spanning four decades from 10^{-8} to 10^{-4}. For a fixed value of χ, as Ca_g increases, so does H_{min}. For a fixed value of Ca_g as χ (or St increases) so does H_{min}. Finally, as χ increases, the variation in H_{min} as the capillary number changes becomes slightly larger; our calculations seem to suggest, however, that these values

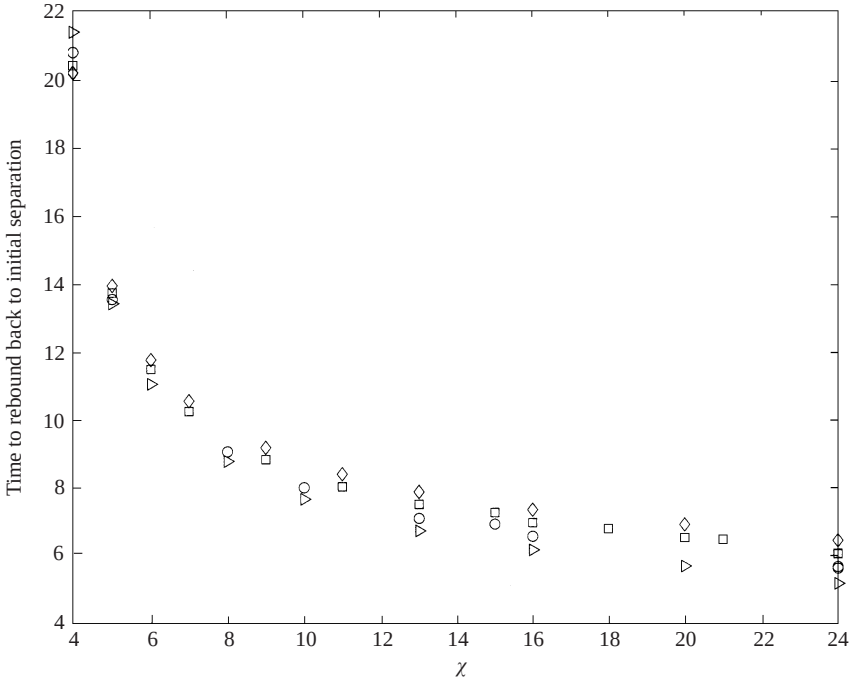

FIGURE 14. Plot of the total scaled time taken by the drops to rebound back to their initial separation of $30(aCa_g^{1/2})$ starting from $t = 0$. ◇, $Ca_g = 10^{-8}$; □, 10^{-7}; ○, 10^{-6}; △, 10^{-5}.

tend to asymptote to constants as the Stokes number increase. Figure 13(b) shows that, for small Stokes numbers (say $\chi = 3$), the centre of mass velocity is positive when the dimple forms, i.e. the drops have already started the rebound process. Thus, the areas of near-contact are moving towards one another while the rear of the drops are receding from each other. The value of the centre of mass velocity when the dimple forms is very weakly dependent on the capillary number – in fact, the collapse for the wide range of Ca_g we consider is quite remarkable. As χ increases, the value of W tends to -1, the deviation from this value is seen to be approximately $O(\chi^{-2})$ in accordance with the behaviour predicted by the equations for small deformation. Thus, for large Stokes numbers, the small deformation that occurs prior to the dimple formation leads to negligible energy storage. Figure 14 shows the total time (scaled by $aWe_d^{1/2}U_c^{-1}$) taken by the drops to rebound back to their initial separation of $30(aCa_g^{1/2})$ starting from $t = 0$. The calculations are for capillary numbers of 10^{-8}, 10^{-7}, 10^{-6} and 10^{-5}. We note that the spread in values increases as the Stokes number increases. Also, at very small values of χ (say 4), collisions characterized by the largest value of Ca_g (10^{-5}) take the longest scaled time. However, as χ increases, this trend is reversed. At $\chi = 24$, the smallest capillary number drops ($Ca_g = 10^{-8}$) take the longest scaled time to complete the collision process. This result is consistent with our idealized bounce calculations where we found that small Weber numbers result in larger scaled bounce times. For small Stokes numbers, the effects of viscous dissipation play an important role and modify this trend.

Figure 15 shows the variation with changing χ in the values of the primary and secondary minimum for two values of the capillary number (10^{-8} and 10^{-6}). As χ increases from small values, the secondary minimum H_{min}^{**} monotonically decreases

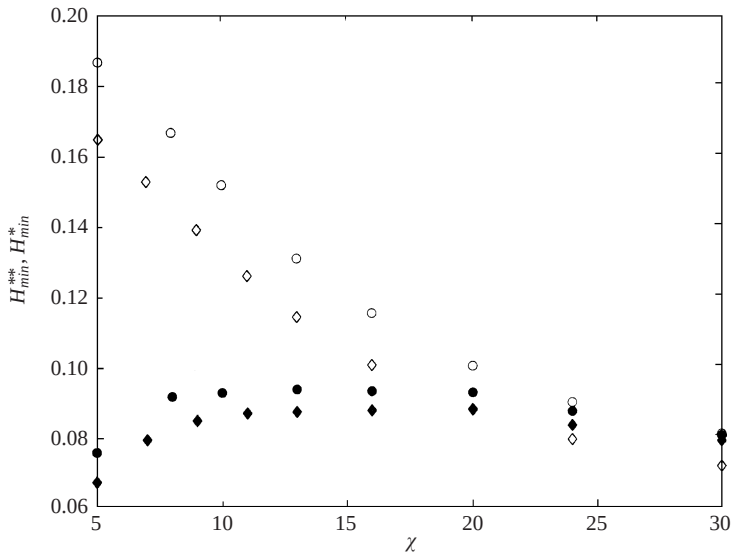

FIGURE 15. Variation of the primary minimum, H^{*}_{min}, (filled symbols) and the secondary minimum, H^{**}_{min}, (open symbols) as the Stokes number is increased. Circles, $Ca_g = 10^{-6}$; diamonds, 10^{-8}.

while the primary minimum H^{*}_{min} increases first, reaches a minimum and then seems to decrease very slowly. Additional calculations for χ in the range 30–40 indicate that the tail minimum H^{*}_{min} remains almost constant and changes by a very small amount compared to the change in the dimple minimum (H^{**}_{min}). Figure 15 clearly indicates that for $\chi \gg 1$, H^{**}_{min} will become comparable to or less than H^{*}_{min}. This transition occurs at a critical Stokes number that depends on Ca_g. Note also that, the smaller the capillary number, the smaller the values of the minima. Rescaling the flux equation (3.5) indicates that the solutions to the equation depend on $\chi^{1/2} \sim O(St^{1/4})$ and hence the rather slow decrease in the dimple minimum as χ increases. Clearly, H^{**}_{min} decreases as χ increases owing to the inertia effect, that is, the drop centroids can come closer for larger Stokes numbers. We also note that the difference in H^{**}_{min} due to varying the capillary number is seen to decrease as the Stokes number increases, indicating that the Weber number effect is more important insofar as the bounce dynamics goes.

4.4. *Coefficients of restitution, bounce times and dimple widths – comparison to idealized bounce problem of § 2.*

In § 2, we studied an idealized bounce problem where dissipation in the gas film was neglected. In other words, the results we obtained correspond to the limit $\mu_g \to 0$, i.e. $Ca_g \to 0$. In this context, the constant $2\sigma/a$ pressure that prevented the near-contact regions from touching is a disjoining force that we specify as acting on the drops. It is illuminating to compare the values for the scaled bounce time, maximum dimple width and coefficients of restitution for small but finite values of Ca_g with the zero capillary number limit.

Let us define a modified bounce time, T_d, as the scaled time for which the dimple exists. In other words, T_d = (scaled time to dimple relaxation) – (scaled time to dimple

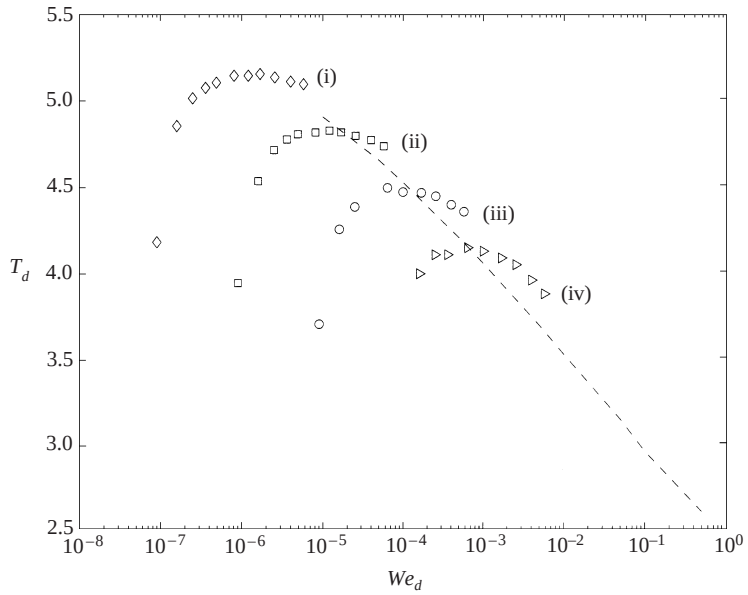

FIGURE 16. The Weber number dependence of the modified bounce time defined as the scaled time for which a dimple exists. – – –, $Ca_g \to 0$ asymptote. ◇, $Ca_g = 10^{-8}$; □, 10^{-7}; ○, 10^{-6}; △, 10^{-5}.

formation). This allows us to correct for the dynamics of the initial trajectory, which in the limit of $St \gg 1$, takes a very short $O(aCa_g^{1/2}U_c^{-1})$ time compared to the much greater $O(aWe_d^{1/2}U_c^{-1})$ time for the dimple to evolve. Furthermore, tail formation and retraction in the limit $St \gg 1$ takes place over a time period that is much smaller than T_d. Thus, T_d is approximately the scaled time for which the centres of the two droplets are closer than $2a$ for $St \gg 1$. Figure 16 shows the Weber number dependence of T_d for Ca_g varying from 10^{-8} to 10^{-5}. The limit of zero viscous dissipation is shown as a dashed curve. For fixed Ca_g, the time T_d increases from zero as χ (or equivalently, the Weber number), increases from zero. The comparative strengths of viscous dissipation and surface deformation dictate the time for which the dimple exists and control the rate of drainage of the gas in the thin film. Consider the results for $Ca_g = 10^{-8}$ denoted by diamonds. For Weber numbers smaller than approximately 10^{-6}, the bounce times are smaller than those predicted by the zero capillary number theory. For small Stokes numbers, most of the initial kinetic energy is dissipated in the gas film; consequently, the energy available for surface deformation is reduced. We could try to correct for this effect by using the Stokes number based on the velocity when the dimple first forms. In addition, the dimple that eventually forms is not very pronounced and relaxes quickly. As χ increases, the drops deform rather than force the gas out of the gap and the gap separation remains almost constant over the time the dimple evolves. Thus, for large Stokes number we expect T_d to approach and follow the dashed line. For a fixed Weber number, the smaller the Stokes number, the smaller the capillary number and so the dimple formation takes place at smaller separations. Thus the smaller film thickness at the rim of the dimple leads to a larger resistance to change in the film thickness.

Figure 17 shows the maximum dimple width scaled with the undeformed drop radius a as a function of We_d for different values of Ca_g. The dashed line is the limiting result corresponding to zero capillary number and provides an upper bound

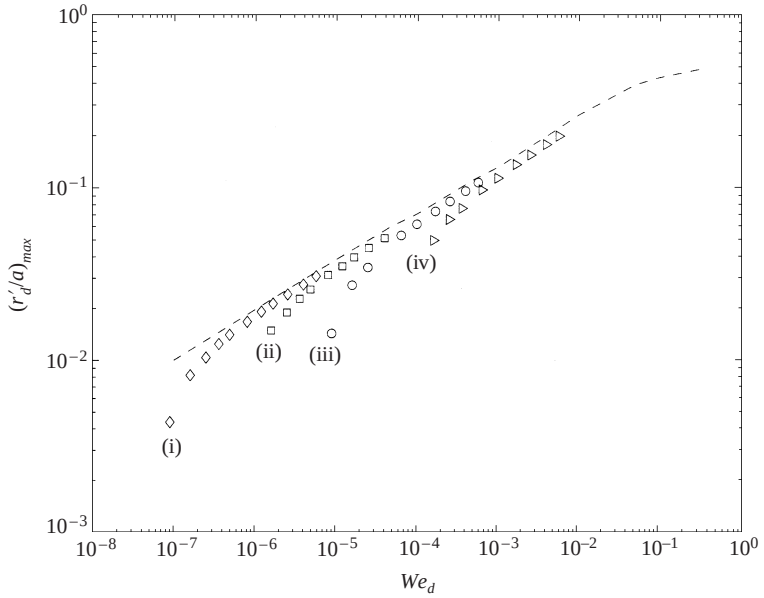

FIGURE 17. The Weber number dependence of the maximum dimple extent for various values of the capillary number, Ca_g. – – –, $Ca_g \to 0$ asymptote. ◇, $Ca = 10^{-8}$; □, 10^{-7}; ○, 10^{-6}; △, 10^{-5}.

to the energy that can be stored as reversible deformation energy. We note that the results for small and finite capillary numbers tend to the zero capillary number limit as the Weber number increases from zero. The range of Weber number over which this agreement is seen increases as $Ca_g \to 0$.

A variable that is usually of most interest in practical applications is the net energy loss in the collision characterized by the coefficient of restitution. In collisions of rigid spheres all the initial energy is dissipated and no rebound occurs. In our previous work (Gopinath *et al.* 1997), we found that rigid spheres colliding in a weakly compressible gas exhibited a rebound for a small range of Stokes numbers. The drops rebound to a much larger extent with almost no loss of energy for $St \gg 1$ ($\chi \gg 1$) and, in fact, rebound back beyond their initial separation. This behaviour is more in line with what is observed in elasto-hydrodynamic collisions of weakly elastic solid spheres in a liquid.

Figure 18 shows the scaled centre of mass speed when the rebound is complete, i.e. when the drops rebound back to their initial separation. The variable plotted is thus $|W'/W'(t = 0)|$ and can be considered the coefficient of restitution for the collision process. We show results of our numerical experiments for two sets of data – the unfilled symbols represent calculations for drop–drop collisions and the filled symbols represent results for a drop colliding with a rigid, planar surface. For both drop–drop and drop–surface calculations, the initial conditions were $h(t = 0) = 15$ and $W(t = 0) = -1$. Also, the drops were assumed to be undeformed at $t = 0$. First, we observe that the dependence on the capillary number is rather weak. In fact, it is only for large values of χ that the data sets for different Ca_g seem to deviate from one another. For a finite capillary number and $\chi \sim O(1)$, a large fraction of the initial energy is dissipated by viscous effects and the coefficient of restitution is small. The effects of dissipation becomes less important as χ increases, indicating that surface deformation is an efficient mechanism to store a large fraction of the initial energy. Note also that for $\chi \gg 1$, smaller capillary numbers lead to larger

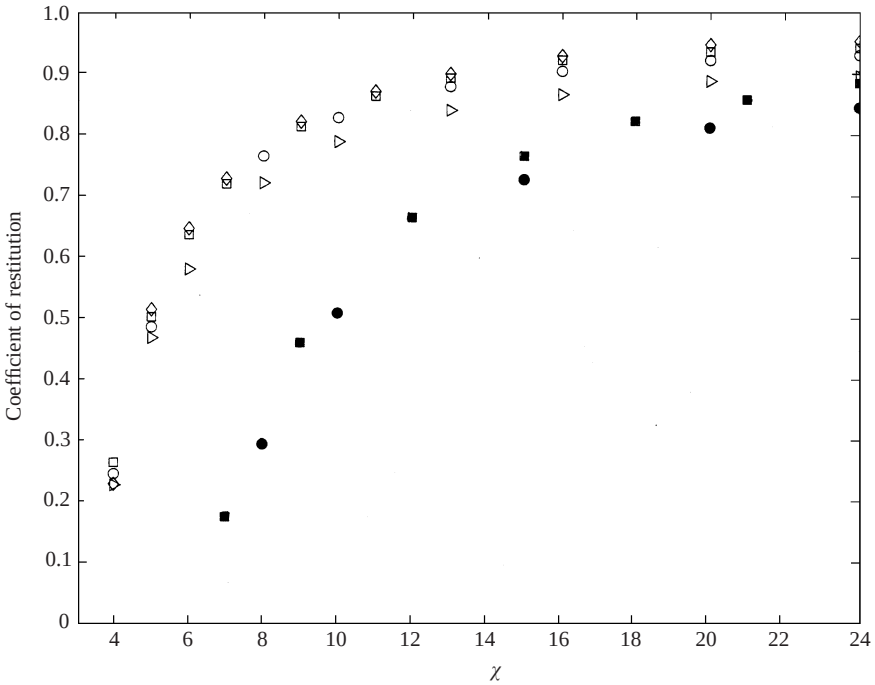

FIGURE 18. Final scaled rebound speeds, (effective coefficient of restitution) as a function of $\chi = (We_d/Ca_g)^{1/2}$ for drop–drop (unfilled symbols) and drop–rigid surface (filled symbols) collisions. ◇, $Ca_g = 10^{-8}$; □, 10^{-7}; ○, 10^{-6}; ▷, 10^{-5}.

scaled rebound velocities, i.e. deformation effects dominate viscous effects. For all the capillary numbers considered, rebound to the initial separation occurred so long as $\chi > 3$. For smaller Stokes numbers, the drops came to a rest after executing damped oscillations. The results for drops colliding with a rigid surface (filled symbols and same notation) illustrate the increased dissipation that occurs owing to the no-slip condition at the rigid surface. For drop–drop collision, this is replaced by a plane of symmetry with a no-stress condition and hence the dissipation is less. As the Stokes number increases this difference in the boundary condition plays less of a role in determining the time scale of the bounce and the coefficient of restitution. Comparison of these results with the energy loss in the idealized collision process of § 2 indicates that even in the limit $Ca_g \ll 1$, viscous dissipation cannot be neglected for $St \leqslant O(1)$.

In the model we have developed and used, the near-contact deformed surfaces are assumed to have a large radius of curvature so that the lubrication, thin-film equations apply. For the Stokes numbers considered in this paper, the lubrication assumption was indeed satisfied for the duration of the collision and rebound process. Our numerical results, however, do indicate that there is a possibility that this might not be valid, albeit for a very short period of time during the tail retraction period when the curvature at $r = 0$ becomes very large. However, the total time this phenomenon takes is negligible compared to the time over which the dimple evolves and the energy dissipation during this time period is expected to be small. Since the collision is assumed to occur in an incompressible continuum gas, the gross dynamical quantities, namely, the force and velocity, will not change very much in this time period.

5. Concluding remarks

In this paper, we analysed the head-on collision and subsequent rebound of two weakly deformable droplets in an incompressible continuum gas. Our results are applicable when the Weber number based on the drop density $We_d \equiv \rho_d U_c'^2 a/\sigma \ll 1$ and the capillary number based on the gas viscosity $Ca_g \equiv \mu_g U_c'/\sigma \ll 1$. The Reynolds number based on drop properties $Re_d \equiv aU_c'\rho_d/\mu_d \gg We_d^{1/2}$.

In the first part of the paper, we analysed an idealized model of the bounce process valid when viscous dissipation in the gas and in the drop can be ignored. We assumed that the only effect of the gas was to supply a constant disjoining pressure to keep the drop interfaces from touching. Such a description is valid provided that the rate of film drainage is so slow that in the time it takes for the drops to rebound, the film thickness remains almost constant. For very small Weber numbers, we used singular perturbation methods to obtain a fully analytic description of the rebound process. Expressions for the rebound times and the extent over which surface flattening occurs were seen to match extremely well with exact simulations and available experimental data.

In the second part of the paper, we obtained the set of equations that provided a more complete picture of the collision process. The analysis took into account the flow in the drop and also in the thin gap separating the drops. These equations were then solved numerically using a semi-implicit, direct, matrix inversion technique. The effects of viscous dissipation due to the flow of the gas out of the gap was studied in detail by varying the capillary number Ca_g. For large Stokes numbers and in the limit $Ca_g \ll 1$, our calculations present the following picture of the approach and rebound process. (i) During the initial approach when $h' \gg O(aCa_g^{1/2})$, the drops approach each other with negligible deformation. The minimum gap thickness occurs at the centreline. (ii) When the minimum gap thickness becomes $O(aCa_g^{1/2})$, the interfaces in the inner region begin to flatten and deform significantly. A dimple then forms. The film thickness at the rim decreases faster than the gap thickness at the centre of the dimple. Meanwhile, the centre of mass velocity of the drop decreases with time as a part of the initial kinetic energy is channelled into deformation energy, a part is stored in the pressure and velocity fields in the interior of the drop and the remainder is dissipated due to gas viscosity. (iii) The centroids of the drops come to rest momentarily and then reverse direction as the rebound process begins. Meanwhile, the minimum gap thickness that occurs at the dimple rim increases as the dimple reaches its maximum extent and begins to shrink. By this time, most of the deformation energy is converted back to the kinetic energy associated with the centre of mass motion. (iv) The edges of the dimple peel away as the drops recede. The minimum gap thickness occurs at the centreline and a tail forms. The rapid motion of the interfaces causes the pressure beyond the rim of the dimple to fall below the ambient value. The flux of gas out of the dimple that develops combined with surface oscillations cause the thickness at the tip of the tail to decrease with time. The centreline separation reaches a minimum and then increases rapidly as the tail retracts. This retraction takes place over a time scale that is very small compared to the time over which the dimple evolves and relaxes. (v) Once retraction is complete, the drops move away from each other. The velocity of the centre of mass of each drop increases, reaches a maximum and then decreases as viscous dissipation becomes important in the final stages of rebound.

Studies on elastohydrodynamic collisions of deformable solid spheres in an incompressible liquid by Davis and co-workers (Davis *et al.* 1986; Serayssol & Davis

1986) showed that two dimensionless parameters influenced the dynamical character of the collision process – an elasticity parameter that characterizes the tendency of the spheres to deform and the Stokes number. For small Stokes numbers, deformation as well as the rebound height was seen to increase as the Stokes number increased. Also, the spheres underwent damped oscillations before finally coming to rest. For Stokes numbers larger than a critical value dictated by the length scale at which deformation became important, the spheres rebounded very strongly. The minimum gap thickness attained scaled by the characteristic length scale at which elastic deformation became important tended to a constant as $St \to \infty$. Most of the initial energy was stored as reversible elastic strain energy and was released during the rebound. In the time period over which the rebound occurred, the gap thickness and the pressure in the gap remained nearly constant. Thus, although the equations governing the elastic deformation of a solid body are very different from those governing the deformation of a liquid–gas interface, we find that the dynamical behaviour is similar to what we observe in collisions between drops. One main difference is that in a drop–drop collision, the whole drop surface deforms: the elastic spheres undergo localized deformation in the region of close contact only.

We considered Stokes numbers of up to 200 in this analysis. Our results indicate that both H^{**}_{min} and H^{*}_{min} vary extremely slowly with the Stokes number in the limit $St \to \infty$. In fact, the results plotted in figure 15 indicate that H^{**}_{min} scales as χ^{a} where the exponent a is about -0.5 when $\chi \sim 20$–30. The Stokes number dependence of the primary minimum exhibits an even weaker dependence on the Stokes number.

The collision orientation we studied was axisymmetric about the line joining the centroids of the drops. Since the gas film exerts only resisting forces and no interparticle attractive forces are present, we do not expect to have unbounded growth of randomly induced surface oscillations. Based on the physics of the problem, it is reasonable to expect that the gas film will be stable to random perturbations – axial and transverse.

As mentioned before, collisions occurring in a continuum incompressible gas cannot end in contact due to the nature of the resisting lubrication force. Two physically relevant mechanisms causing lubrication breakdown are compressibility of the gas and/or non-continuum effects. Compressibility effects will become important when the pressure drop along the gap becomes comparable to the outside ambient pressure. Consider the case of a collision between two identical rigid spheres moving towards each other with equal speeds. Using the scaling of the pressure for incompressible lubrication flow, $p' = O(\mu_g U'_c a/h'^2)$, h' being the minimum gap thickness, we can obtain an estimate of the relevant length, h_c, at which compressibility effects become important. This is given by $h'_c \equiv (2\mu_g U'_c a/p'_\infty)^{1/2}$ where p'_∞ is the ambient pressure. When the particle separation is comparable to or smaller than h'_c the relative motion of the surfaces will cause the gas to compress rather than flow out (Gopinath *et al.* 1997). Alternatively, when the gap between the particles becomes comparable to the mean free path of the molecules, λ_o, the description of the gas as a continuum breaks down and non-continuum effects have to be taken into account. For example, the mean free path of air molecules is approximately 0.05 μm and colliding drops would approach to distances smaller than this value. The Navier–Stokes equation is then inadequate to represent the gas flow. We have to use the Boltzmann equation which governs the evolution of the probability density of the gas. If the colliding drops have infinite surface tension (rigid spheres) lubrication breakdown will allow contact to occur in finite time provided the drops have sufficient energy as shown in studies by (Sundararajakumar & Koch 1996; Gopinath *et al.* 1997). When drop deformation is

taken into consideration we see clearly that the collision outcome is determined by the relative importance of two competing effects – drop deformation which tends to store energy and cause rebound, and lubrication breakdown mechanisms that allow for contact to occur. In a subsequent publication, we will explore these in detail using a formulation similar to that presented in this paper.

This work was supported by the US Environmental Protection Agency under grant number R827115. The authors would like to thank Dr Alexander Zinchenko for help with his thin film code and also for very useful and interesting discussions.

Appendix A. Scaling arguments used in the derivation of governing equations

A.1. *Validation of basis function expansion*

Examination of the linear operator Υ_o shows that if $\mathscr{H} = \mathscr{H}_{sol}$ is a solution to the operator equation $\Upsilon_o\mathscr{H} = \psi(\eta, t)$ then so is $\mathscr{H} = \mathscr{H}_{sol} + \gamma_1(t)\eta + \gamma_2(t)\mathscr{F}(-\frac{1}{2}, 1, \frac{1}{2}, \eta^2)$, $\gamma_1(t)$ and $\gamma_2(t)$ being appropriately chosen functions of time. Here $\mathscr{F}(-\frac{1}{2}, 1, \frac{1}{2}, \eta^2)$ is a generalized hypergeometric function and is logarithmically singular at $\eta = \pm 1$. We note now that since there are no sinks or sources of mass or momentum in the drop, the velocity potential ϕ has to be bounded at all points in the drop interior. The kinematic interface condition combined with the Laplace equation for the velocity potential suggests that the rate at which deformation occurs should also be bounded at points on the drop surface. At the point diametrically opposite to the point of close contact, i.e. at $\eta = -1$, the drop deformation should be small and bounded. Since we have specified that the interface be flat over the region $\theta = 0$ to $\theta = \alpha$, the matching is actually carried out at the edge of the dimple, namely, at $\eta = \cos\alpha$ where $\mathscr{F}(-\frac{1}{2}, 1, \frac{1}{2}, \eta^2)$ is bounded. In addition, at the start of the collision process, i.e. at $t = 0$, the dimple extent is zero and so the drops are exactly spherical correct to $O(We_d^{1/2})$. These conditions, together with the criterion that the velocity potential should be bounded, allow us to write $\mathscr{H}$ as a linear superposition of a set of complete and bounded basis functions. The regular parts of the homogeneous solutions can then be rewritten in terms of these basis functions too.

A.2. *Outer trajectory scaling*

The outer trajectory calculations are started when the drops are separated by a distance equal to $O(a)$ and are undeformed. At inter-drop distances of $O(a)$, the gas flow around the drops is governed by the Stokes equations provided $St < O(\rho_d/\rho_g)$. As the drops converge, the dynamic pressure that is created in the gas scales roughly as $O(\mu_g U_c'/a)$. For $St \gg 1$, the centre of mass speeds do not change much in the time it takes for the separation to reduce to a value that marks the beginning of the lubrication regime. The centre of mass velocity of the drops relaxes on a viscous timescale $\tau_v \sim 2\rho_d a^2(9\mu_g)^{-1}$. The characteristic magnitude of the deformation induced velocities is $u_f \ll U_c'$ and this velocity evolves over a time scale $\tau_c \sim O(a/U_c') \ll \tau_v$. Because the governing equations for Stokes flow are quasi-steady and linear, the pressure and the velocity fields set up in the gas at any given time are completely determined by instantaneous velocities and position of the interfaces. To leading order, the deformation of the surface is small compared to the radius a and may be neglected. Similarly, the velocity of each drop–gas interface is approximately equal to the velocity of the centroid of the corresponding drop. The deformation in the outer trajectory becomes important only for moderately small or $O(1)$ values of $Ca_g^{1/2}$;

in these cases, we can neglect any induced tangential velocity of the surfaces. The pressure and velocity fields in the gas can be obtained by solving for the flow around two rigid spheres moving towards each other with specified velocities. These velocities are in turn determined by the overall hydrodynamic force acting on the drops.

We write the drop velocity as $\boldsymbol{u}'_d(\boldsymbol{r}', t') = \boldsymbol{u}'_{cm}(t') + \boldsymbol{u}'_f(\boldsymbol{r}', t')$ where $u'_{cm}(t') \sim O(U'_c)$ and $u'_f \ll u'_{cm}(t')$. The part $\boldsymbol{u}'_f(\boldsymbol{r}', t')$ is the deformation induced velocity and is small compared to the centre of mass velocity. Then,

$$\rho_d \frac{\partial \boldsymbol{u}'_{cm}}{\partial t'} \sim O\left(\rho_d \frac{U'_c}{\tau_v}\right), \quad \rho_d \frac{\partial \boldsymbol{u}'_f}{\partial t'} \sim O\left(\rho_d \frac{U'_c}{\tau_v}\frac{\tau_v}{\tau_c}\frac{u_f}{U'_c}\right), \quad \rho_d \boldsymbol{u}'_{cm} \cdot \nabla' \boldsymbol{u}'_f \sim O\left(\rho_d \frac{U'_c}{\tau_v}\frac{\tau_v}{\tau_c}\frac{u_f}{U'_c}\right)$$

$$\rho_d \boldsymbol{u}'_f \cdot \nabla' \boldsymbol{u}'_f \sim O\left(\rho_d \frac{U'_c}{\tau_v}\frac{\tau_v}{\tau_c}\left(\frac{u_f}{U'_c}\right)^2\right), \quad \mu_d \Delta' \boldsymbol{u}'_f \sim O\left(\rho_d \frac{U'_c}{\tau_v}\frac{\tau_v}{\tau_c}\frac{u_f}{U'_c} Re_d^{-1}\right).$$

When $Re_d \gg 1$, the viscous term can be neglected in comparison to other terms. The Stokes number, $St \sim \tau_c/\tau_v > 1$. For $Re_d \gg 1$ and $St \gg 1$, the flow induced in the drop due to deformation and surface stress is less than the centre of mass speed, namely, $u_f/U'_c \ll 1$, the nonlinear quadratic inertial term $\boldsymbol{u}'_f \cdot \nabla' \boldsymbol{u}'_f$ may be neglected. For Stokes numbers $1 \ll St \ll Ca_g^{-1}$, the capillary pressure balances the external gas pressure $O(\mu_g U'_c/a)$; thus, the deformation is $O(aCa_g)$ and $u_f \sim O(U'_c Ca_g) \ll U'_c$. For the dynamic drop pressure to be of the same order as this gas pressure, we require that $p'_d = p'_o + 2\sigma/a + O(a\rho_d U'_c \tau_v^{-1})$ and the governing equation then attains the simple form:

$$\rho_d \frac{\partial \boldsymbol{u}'_{cm}}{\partial t'} + \nabla' p'_d = 0.$$

This equation applies even for moderately large or $O(1)$ drop Reynolds numbers. When $St \sim O(1)$ and for moderately small capillary numbers say, $Ca_g \sim O(0.1)$, we expect that the induced flow occurring inside the drop should be included in our analysis. Scaling time with t_c and the dynamic pressure with $\mu_g U'_c/a$ we obtain:

$$\frac{We_d}{Ca_g}\left(\frac{\mathrm{d}\boldsymbol{u}_{cm}}{\mathrm{d}t}\right) + We_d\left[\frac{\partial \boldsymbol{u}_f}{\partial t} + \boldsymbol{u}_{cm} \cdot \nabla \boldsymbol{u}_f\right] = -\nabla P_d.$$

Here, we have assumed (subject to verification) that $u_f = U'_c Ca_g$. Note that the net force on each drop scales like $O(\mu_g U'_c a)$. The first term on the left-hand side is actually $O(1)$ whereas the other terms on the left-hand side are $O(We_d) < 1$. Thus, as long as $St \geqslant O(1)$ and $We_d < 1$, the main contribution to the pressure gradient in the drop comes from the net force acting on the drop and we need not consider the flow inside the drop to calculate the deformation to leading order – just the net force acting on the drop due to the gas outside will suffice. The correction to the leading-order $O(1)$ term becomes increasingly important and u_f becomes of the order of U'_c. As a check of consistency, we note that for $We_d \leqslant 1$, the deformation is $O(aCa_g)$ and the characteristic velocity is indeed $O(U'_c Ca_g)$ as is assumed in the scaling.

A.3. *Alternative derivation of outer equations*

In deriving equation (3.23) we have neglected higher-order terms that vanish as $Ca_g \to 0$. An additional condition that results is that $r^2(Ca_g/We_d)^{1/2} \gg 1 + \ln[r^2(Ca_g/We_d)^{1/2}]/2$. A physical interpretation of this criterion is that the deformation at the outer edge of the lubrication layer and in the matching region, should be small compared to the undeformed radius. We may also derive equation (3.23) in

a manner comparable to the analysis in § 2. We consider a mean constant pressure of value equal to $\frac{4}{3}\rho_d U_c^2 We_d^{-1/2}(\sin\alpha)^{-2}\mathrm{d}W/\mathrm{d}t$ acting over a flat region of radial extent $(a\sin\alpha)$. Using this step function form for the pressure profile in (3.22), we can write down the rate at which the velocity in the drop changes. In the limit $\alpha \to 0$, we find, as expected, that only the net force acting in the inner region determines the deformation in the outer region and details of the deformation in the inner region are not important.

Appendix B. Numerical methodology

B.1. *Numerical scheme and discretization*

The first order, implicit (backward) Euler scheme for the time derivative and central differences for the radial derivative were used to solve the equations. The implicit time-stepping scheme renders the numerical computation stable whereas the central differencing adopted allows for second-order accuracy in space.

First, we discretize the equations at points r_i; $i = 1, 2, \ldots, N+1$ where r_{N+1} is the last grid point selected such that the asymptotic form for the deformation is satisfied. Then, given the gap profile H^n, pressure p_g^n, force F^n, velocity W^n and h^n at the nth time level, the equation for the flux, namely (3.5), was made semi-implicit and linear in H^{n+1} and p_g^{n+1} thus:

$$\frac{1}{r}\frac{\partial}{\partial r}\left[r(H^3)^n\left(\frac{\partial p_g}{\partial r}\right)^{n+1}\right] = 24\mathscr{Q}^{n+1} = 24\frac{1}{\chi}\left(\frac{\mathscr{Y}^{n+1}-\mathscr{Y}^n}{\mathrm{d}t}\right), \tag{B 1}$$

where

$$\mathscr{Y}^{n+1} = h^{n+1} + \chi D^{n+1} = h^{n+1} + \left(\frac{We_d}{Ca_g}\right)^{1/2} D^{n+1}, \tag{B 2}$$

$$\mathscr{Q}^{n+1} = W^{n+1} + \left(\frac{\mathrm{d}D}{\mathrm{d}t}\right)^{n+1} = \frac{1}{\chi}\left(\frac{\mathrm{d}\mathscr{Y}}{\mathrm{d}t}\right)^{n+1}, \tag{B 3}$$

so that

$$H^{n+1} = 2\mathscr{Y}^{n+1} + r^2. \tag{B 4}$$

The time rates of change of h and W are given by:

$$\left(\frac{\mathrm{d}h}{\mathrm{d}t}\right)^{n+1} = \frac{h^{n+1}-h^n}{\mathrm{d}t} = \chi W^{n+1} \tag{B 5}$$

and

$$\left(\frac{\mathrm{d}W}{\mathrm{d}t}\right)^{n+1} = \frac{3}{2\chi}\int_0^{r_\infty} p_g^{n+1} r\,\mathrm{d}r = \frac{W^{n+1}-W^n}{\mathrm{d}t}. \tag{B 6}$$

We have set the pressure at infinity, p_∞, to be zero for convenience and we also take the limit $r_\infty \to \infty$ when evaluating the force. The Young–Laplace equation is evaluated thus:

$$\frac{1}{r}\frac{\partial}{\partial r}\left(r\frac{\partial \mathscr{Y}}{\partial r}\right)^{n+1} = -p_g^{n+1}. \tag{B 7}$$

This procedure parallels that used in the paper by Rother *et al.* (1997) and is similar to the linearization process advocated by Lees (1966). In addition, the equations for

$\mathscr{L}_k$ and B_k are differenced as (for $k \geqslant 2$)

$$\left(\frac{\mathrm{d}\mathscr{L}_k}{\mathrm{d}t}\right)^{n+1} = \frac{\mathscr{L}_k^{n+1} - \mathscr{L}_k^n}{\mathrm{d}t} = kB_k^{n+1}, \tag{B 8}$$

$$\left(\frac{\mathrm{d}B_k}{\mathrm{d}t}\right)^{n+1} = \frac{B_k^{n+1} - B_k^n}{\mathrm{d}t} = -(k^2 + k - 2)\,\mathscr{L}_k^{n+1} - \frac{2k+1}{3}\left(\frac{\mathrm{d}W}{\mathrm{d}t}\right)^{n+1}. \tag{B 9}$$

The boundary conditions on the variables p_g and $\mathscr{Y}$ are given by:

$$p_g^{n+1}(r_{N+1}) = \frac{-3}{r_{N+1}^4}\mathscr{Q}^{n+1}(r_{N+1}) \tag{B 10}$$

and

$$\mathscr{Y}^{n+1}(r_{N+1}) = h^{n+1} + \chi D^{n+1}(r_{N+1}), \tag{B 11}$$

where

$$D^{n+1}(r_{N+1}) = -\frac{2}{3}\left(\frac{\mathrm{d}W}{\mathrm{d}t}\right)^{n+1}\ln(r_{N+1}) + f^{n+1}(t), \tag{B 12}$$

and the constant f^{n+1} is evaluated using (3.27) and (3.28). Now integrating (B 1) twice over r, using the symmetry condition at $r = 0$ and equation (B 10), changing the order of integration and finally discretizing using the trapezoidal rule we obtain a matrix equation relating p_g^{n+1} to $\mathscr{Q}^{n+1}$ of the form $\boldsymbol{p}_g^{n+1} = \boldsymbol{E}\cdot\boldsymbol{Q}^{n+1}$. Similarly, integrating (B 7) twice over r, imposing the symmetry condition at the origin and using the matrix form for the pressure we obtain an equation for $\boldsymbol{Y}^{n+1}$ in terms of $\mathscr{Y}^{n+1}(r = 0, t)$ and p_g^{n+1}. Here, the elements of $\boldsymbol{p}_g^{n+1}$, $\boldsymbol{Q}^{n+1}$ and $\boldsymbol{Y}^{n+1}$ are values of p_g, $\mathscr{Q}$ and $\mathscr{Y}$ at grid points $r_i, i = 1, 2, \ldots, N+1$ where the last grid point is r_{N+1}. Using these matrix equations, we finally obtain a matrix equation for $\boldsymbol{Q}^{n+1}$:

$$\boldsymbol{S}\cdot\boldsymbol{Q}^{n+1} = -\boldsymbol{Y}^n + \mathscr{Y}^{n+1}(r = 0, t)\mathbf{1}, \tag{B 13}$$

where $\boldsymbol{S}$ is obtained by substituting the matrix form of (B 1) into the matrix form of (B 7). Note that $\mathscr{Y}^{n+1}(r = 0, t)$ is as yet unknown. The solution to (B 13) is written as $\boldsymbol{Q}^{n+1} = \boldsymbol{Q}_1^{n+1} + \mathscr{Y}^{n+1}(r = 0, t)\boldsymbol{Q}_2^{n+1}$ where

$$\boldsymbol{S}\cdot\boldsymbol{Q}_1^{n+1} = -\boldsymbol{Y}^n, \quad \boldsymbol{S}\cdot\boldsymbol{Q}_2^{n+1} = \mathbf{1}. \tag{B 14}$$

These equations may then be used to obtain an algebraic equation for the unknown gap width $\mathscr{Y}^{n+1}(r = 0, t)$. This, when known, can be substituted back to find $\mathscr{Q}^{n+1}$ and hence $\mathscr{Y}^{n+1}, p_g^{n+1}, W^{n+1}, F^{n+1}, h^{n+1}$ and H^{n+1}. It should be pointed out that the direct semi-implicit scheme has some similarities to the three-level scheme proposed by Lees (1966) to solve quasi-linear parabolic equations. The algorithm proposed by Rother *et al.* achieves linearization of the governing equations in a similar manner; however, because backward (implicit) Euler differencing is used for the time derivatives and central differences for the space derivatives, the complicated boundary condition on the gap thickness at large r can be implemented easily.

The accuracy of the numerical method was checked by comparing the solutions obtained at different values of Δt and Δr. Varying Δt allows us to test the temporal accuracy of the solutions while varying Δr allows us to probe the effect of grid resolution. In our calculations, the last grid point was chosen such that the asymptotic expression for the deformation was readily satisfied. We used a mesh with a fixed number of grid points but varying grid size in order to make sure that deformation and pressure gradients were resolved accurately. The mesh contracted as the drops

came closer to one another and expanded as the drops receded from each other. The mesh size was made constant as soon as the dimple formed and remained constant until the dimple vanished. Most calculations were carried out with 251 grid points. Calculations with 151–601 grid points showed nearly identical results with variations in rebound times and minimum gap thickness of less than 2%. The cutoff value for the last grid point was calculated as $r_{sc}[H_{min}(t)/2]^{1/2}$ where r_{sc} is a scaling coefficient. Most calculations used $r_{sc} = 20$ so that the last point was sufficiently larger than the maximum dimple width. Values of r_{sc} in the range 10–30 resulted in the same values of all dynamical quantities. We note that the pressure decays very rapidly beyond the dimple and hence the cutoff radius does not have to be much larger than the dimple extent. Typical values of the time increment Δt used ranged from $10^{-1}/5$–$10^{-2}/5$. In all cases, we made sure that converged results were obtained. A small time step was used in the tail formation and retraction step so that the fast dynamics of tail retraction could be adequately captured. Finally, the cutoff number for the outer modes we used were $N_c = 3$–4 for $\chi \sim O(1)$ and $N_c = 5$–7 for $\chi \gg 1$.

B.2. *Validation of numerical code: application to collision of a deformable drop with a rigid wall owing to the action of a constant force*

In order to validate the numerical code and test its accuracy and convergence properties, we analysed the buoyancy driven collision of a deformable drop with a rigid flat wall in the presence of a gas. This corresponds to zero Stokes number (no drop inertia) and a constant body force. Numerical results for the film thickness and pressure profiles obtained from our code were compared with those obtained by a completely different method by Yiantsios & Davis (1990). The equations we solve (in dimensionless form) are:

$$\frac{1}{r^*}\frac{\partial}{\partial r^*}\left[r^* H^{*3}\left(\frac{\partial p^*}{\partial r^*}\right)\right] = \frac{\partial Y^*}{\partial t^*} \tag{B 15}$$

$$\frac{1}{r^*}\frac{\partial}{\partial r^*}\left(r^*\frac{\partial Y^*}{\partial r^*}\right) = -p^* \tag{B 16}$$

and

$$\frac{2}{3} = \int_0^\infty p^* r^* \mathrm{d}r^*, \tag{B 17}$$

with

$$H^* = Y^* + \tfrac{1}{3}r^{*2}. \tag{B 18}$$

Here, p^* is the scaled gas pressure and H^* is the scaled gap thickness. Flow of the liquid inside the drop may be neglected in this case. In this case too, we find that for large r^*, the deformation diverges as $\ln r^*$ and the $O(1)$ constant required to determine the deformation far from the lubrication region is obtained from equation (B 17).

In accordance with the initial conditions used by Yiantsios & Davis, we started our calculations with $Y^* = 20$ and traced the trajectory of the drop over several decades in time. We used a contracting mesh with 200 grid points and a dimensionless step size $\mathrm{d}t^* = 10^{-1}$. The results using a step size $\mathrm{d}t^* = 10^{-2}$ and 400 grid points do not change the solution values significantly. Our results for the deformation and pressure profiles at various instants in time compared extremely well with the graphs in Yiantsios & Davis. Figure 19(a) illustrates the validity and accuracy of our calculations compared to Yiantsios & Davis. The two solid lines show the variation of the scaled centreline gap separation, $H^*(r^* = 0, t^*)$, and the minimum gap thickness, $H^*_{min}(t^*)$, respectively.

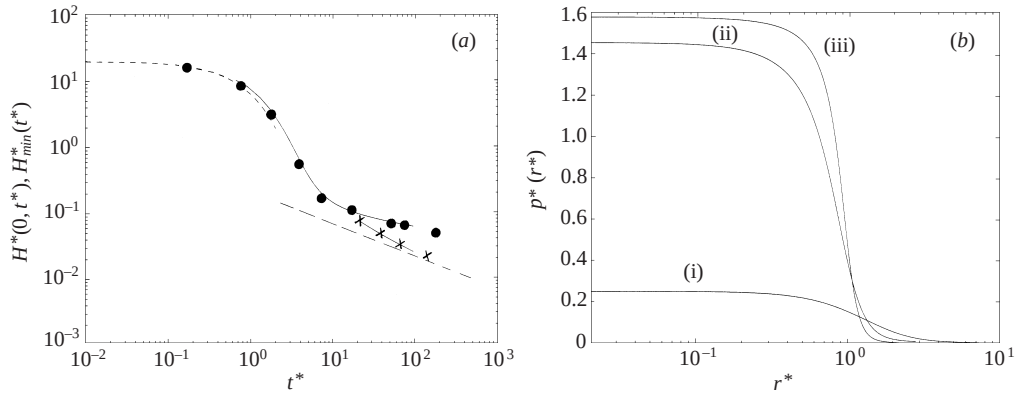

FIGURE 19. (*a*) Temporal evolution of the minimum gap width and the centreline gap width for zero inertia drops colliding due to the action of a constant force (*b*) Profiles of the pressure in the gas film at various instants in time illustrating dimple evolution. Note the steepening of the pressure profile leading to a sharper pressure gradient at the rim as time increases.

The line with short dashes is a regular perturbation, asymptotic solution valid for small deformations (small times) and the line with long dashes is the long-time asymptotic solution for the minimum gap thickness, H^*_{min}, representing the quasi-steady approach of the drop interfaces. This long-time asymptote is given by,

$$H^*_{min}(t^*) \sim 0.4897\ldots(\tfrac{3}{16})^{1/2}t^{*-1/2}.$$

The solid circles and the crosses are numerical results obtained by Yiantsios & Davis using an iterative nonlinear solver. These values were obtained from a visual examination of the graphs in their paper. Note that at short times, a dimple is not formed and so the minimum gap thickness occurs at $r^* = 0$. However, at $t^* \approx 10.0$, a dimple forms and the minimum gap width occurs not at $r^* = 0$, but at the rim of the dimple. Figure 19(*b*) shows the pressure profiles in the gap when $H^*_{min} = 1.0$, 0.10 and 0.05. These pressure profiles match those in Yiantsios & Davis. As the drops come closer, the dimple radius keeps increasing with time and the pressure in the dimple also increases. The pressure gradient at the rim of the dimple becomes larger at the same time. For very large times, the nearly constant pressure in the dimple and the radial extent of the dimple region may be obtained by balancing the lubrication force with the external driving force causing the collision. Calculations indicate that for the initial conditions we adopted, the dimple reaches slightly more than 93% of its maximum extent by a dimensionless time $t^* \approx 75$, a value that agrees with that reported by Yiantsios & Davis. In fact, all our numerical results for the pressure and deformation profiles and the temporal evolution of the dimple radius also match very well with the results of Yiantsios & Davis.

REFERENCES

ASHGRIZ, N. & POO, J. Y. 1990 Coalescence and separation in binary collision of liquid drops. *J. Fluid Mech.* **221**, 183.

BARNOCKY, G. & DAVIS, R. H. 1989 The influence of pressure-dependent density and viscosity on the elastohydrodynamic collision and rebound of two spheres. *J. Fluid Mech.* **209**, 501.

BRADLEY, S. G. & STOW, C. D. 1978 Collision between liquid drops. *Phil. Trans. R. Soc. Lond.* A **287**, 635.

Brazier-Smith, P. R., Jennings, S. G. & Latham, J. 1972 The interaction of falling water drops: coalescence. *Proc. R. Soc. Lond.* A **326**, 393.

Davis, R. H., Schonberg, J. A. & Rallison, J. M. 1989 The lubrication force between two viscous drops. *Phys. Fluids* A **1**, 77.

Davis, R. H., Serayssol, J.-M. & Hinch, E. J. 1986 The elastohydrodynamic collision of two spheres. *J. Fluid Mech.* **163**, 479.

Foote, G. B. 1975 The water drop rebound problem: dynamics of collision. *J. Atmos. Sci.* **32**, 390.

Friedlander, S. K. 1977 *Smoke, Dust and Haze: Fundamentals of Aerosol behavior*. Wiley.

Fuchs, N. A. 1964 *The Mechanics of Aerosols*. Pergamon.

Gopinath, A., Chen, S. B. & Koch, D. L. 1997 Lubrication flows between spherical particles colliding in a compressible non-continuum gas. *J. Fluid Mech.* **344**, 245.

Hidy, G. M. & Brock, J. R. 1970 *The Dynamics of Aerocolloidal Systems*. Pergamon.

Jayaratne, O. W. & Mason, B. J. 1964 The coalescence and bouncing of drops at an air/water interface. *Proc. R. Soc. Lond.* A **280**, 545.

Jiang, Y. J., Umemura, A. & Law, C. K. 1992 An experimental investigation on the collision behaviour of hydrocarbon droplets. *J. Fluid Mech.* **234**, 171.

Karl, A. & Frohn, A. 2000 Experimental investigation of the interaction process between droplets and hot walls. *Phys. Fluids* **12**, 785.

Lees, M. 1966 A linear three-level difference scheme for quasilinear parabolic equations. *Math. Comput.* **20**, 516.

Mason, B. J. 1971 *The Physics of Clouds*. Oxford.

Murad, S. & Law, C. K. 1999 Molecular simulation of droplet collision in the presence of ambient gas *Mol. Phys.* **96**, 81.

Nobari, M. R., Jan, Y.-J. & Tryggvason, G. 1996 Head-on collision of drops – a numerical investigation. *Phys. Fluids* **8**, 29.

Ochs, H. T. & Beard, K. V. 1985 Effects of coalescence efficiencies on the formation of precipitation. *J. Atmos. Sci.* **42**, 1451.

Ochs, H. T., Czys, R. R. & Beard, K. V. 1980 Laboratory measurements of coalescence efficiencies for small precipitation drops. *J. Atmos. Sci.* **3**, 225.

Park, R. W. 1970 Behaviour of water drops colliding in humid nitrogen. PhD thesis, Department of Chemical Engineering, The University of Wisconsin.

Qian, J. & Law, C. K. 1994 Effects of ambient gas pressure on droplet collision. *AIAA Paper AIAA-94-0681*.

Rother, M. A., Zinchenko, A. Z. & Davis, R. H. 1997 Buoyancy-driven coalescence of slightly deformable drops. *J. Fluid Mech.* **346**, 117.

Serayssol, J.-M. & Davis, R. H. 1986 The influence of surface interactions on the elastohydrodynamic collision of two spheres. *J. Coll. Interface Sci.* **114**, 54.

Spengler, J. D. & Gokhale, N. R. 1973 Drop impactions. *J. Appl. Meteorol.* **12**, 316.

Sundararajakumar, R. R. & Koch, D. L. 1996 Non–continuum flows between particles colliding in a gas. *J. Fluid Mech.* **313**, 283.

Tsao, H.-K. & Koch, D. L. 1994 Collisions of slightly deformable, high Reynolds number bubbles with short-range forces. *Phys. Fluids* **6**, 2591.

Wachters, L. H. J. & Westerling, N. A. J. 1966 The heat transfer from a hot wall to impinging water drops in the spheroidal state. *Chem. Engng Sci.* **21**, 1047.

Yao, S.-C. & Cai, K. Y. 1988 The dynamics and Leidenfrost temperature of drops impacting on a hot surface at small angles. *Exp. Therm. Fluid Sci.* **1**, 363.

Yiantsios, S. G. & Davis, R. H. 1990 On the bouyancy-driven motion of a drop towards a rigid surface or a deformable surface. *J. Fluid Mech.* **217**, 547.